

The development of algebraic stress models using a novel evolutionary algorithm



J. Weatheritt^{*,1}, R.D. Sandberg²

Department of Mechanical Engineering, University of Melbourne, Parkville, VIC, 3010, Australia

ARTICLE INFO

Keywords:

RANS modelling
Machine-learning
Evolutionary algorithm
Gene expression programming
Algebraic stress modelling

ABSTRACT

This work presents developments to a novel evolutionary framework that symbolically regresses algebraic forms of the Reynolds stress anisotropy tensor. This work contributes to the growing trend in machine-learning for modelling physical phenomena. Our framework is shown to be computational inexpensive and produce accurate and robust models that are tangible mathematical expressions. This transparency in the result allows us to diagnose issues with the regressed formulae and appropriately make amendments, as we further understand the regression tools. Such models are created using hybrid RANS/LES flow field data and a passive solving of the RANS transport equations to obtain the modelled time scale. This process shows that models can be regressed from a qualitatively correct flow field and fully resolved DNS is not necessarily required. Models are trained and tested using rectangular ducts, an example flow genus that linear RANS models even qualitatively fail to predict correctly. *A priori* and *a posteriori* testing of the new models show that the framework is a viable methodology for RANS closure development. This *a posteriori* agenda includes testing on an asymmetric diffuser, for which the new models vastly outperform the baseline linear model. Therefore this study presents one of the most rigorous and complete CFD validation of machine learnt turbulent stress models to date.

1. Introduction

For many design problems of engineering interest, flow is predicted primarily with Reynolds-Averaged Navier-Stokes (RANS) equations. This is because of the excessive computational effort required for Large Eddy (LES) and Direct Numerical Simulation (DNS) techniques (Hanjalić, 2005). That said, RANS modelling is based on very limiting assumptions that often fall down unexpectedly and with catastrophic repercussions for statistical results on moderately complex geometries (Hunt and Savill, 2005). This is because RANS model uncertainty remains poorly understood (Ling and Templeton, 2015). Particular examples include the now classical periodic hills test case (Temmerman and Leschziner, 2001; Temmerman et al., 2003; Fröhlich et al., 2005) and the asymmetric diffuser of Cherry et al. (2008); 2009). ERCOFTAC Workshops surrounding the former (Jakirlić et al., 2001; Manceau, 2003) and latter (Steiner et al., 2009) show that RANS closures fail to predict even global flow features reliably. For the periodic hills test case, this manifests as poor reverse flow prediction and for the diffuser, separation often occurred from the wrong side of the duct. Note, the periodic hills have been subject to a

recent study (Weatheritt and Sandberg, 2016c), whilst the diffuser is a large focus of this paper.

Because of this high uncertainty, a plethora of RANS methods exist throughout the literature (e.g. Leschziner, 2015) and there is no general consensus on a particular approach. There perhaps may not be a universal RANS closure that outperforms all others for an arbitrary flow configuration (Spalart, 2000). With respect to industry standard, models tend to be variants of the $k - \omega$ -SST (Menter, 1994), $k - \varepsilon$ (Chien, 1982) and Spalart and Allmaras (1994) turbulence closures. These three all utilise a linear stress-strain relationship, despite well known theoretical (e.g. Schmitt, 2007) and practical shortfalls (e.g. Wilcox, 1993), because of its robustness and the uncertainty in more complex approaches (Pope, 1999).

Instead, this work adheres to what (Spalart, 2015) terms, an ‘Openly Empirical’ approach. That is, the turbulence closure aims to correctly model physics but contains no ‘explicit connection’ to the exact turbulence equations. The models proposed in this work are derivatives (not in the formal sense) of high-fidelity data sets. Because of the shortfalls in the linear stress-strain relationship, this is a primary candidate for improvement when developing turbulence closures. Rather

* Corresponding author.

E-mail addresses: jack.weatheritt@unimelb.edu.au (J. Weatheritt), richard.sandberg@unimelb.edu.au (R.D. Sandberg).

¹ Post-doctoral researcher.

² Chair of computational mechanics.

than assuming the task of discovering the universal relationship, we propose a universal framework for specific closure formulation. That is, for a given database one obtains a class of stress-strain relationships suitable for flows at least topologically similar. This is demonstrated in this paper. Changing model coefficients is widely practised for a calculation, using a given model, for a specific flow. In this paper, we generalise to alter the stress-strain functional form. Indeed, many turbulence models have been developed for specific flows, take the examples of jets in crossflow (Bergeles et al., 1978) and turbulent wall jets (Ljuboja and Rodi, 1981). The latter model was developed specifically to overcome the standard model's tuning on free jets. We propose new non-linear stress-strain relationships, known widely as Explicit Algebraic (Reynolds) Stress Models (EASMs or EARSMs) (Pope, 1975; Rodi, 1976), of which many such models exist (e.g. Gatski and Speziale, 1993; Wallin and Johansson, 2000; Craft et al., 2000).

The task of formulating models from data, in the manner presented here, falls under the umbrella of techniques widely known as machine-learning. Applications of such techniques for turbulence model development is a fast growing area of research and we would denote it 'Maximally Empirical', to extend the taxonomy of Spalart (2015). That is, we enforce Galilean invariance — through an integrity basis (Spencer and Rivlin, 1958; 1959) — but beyond this, the machine-learning algorithm is entirely free to formulate mathematical expressions that relate stress to strain.

Similar studies have emerged in previous years which we classify, rather broadly, into: uncertainty quantification, model development demonstrating *a priori* success and model development demonstrating *a posteriori* success. Model development infers some modification to the turbulence closure, whilst we define *a priori* demonstrations as still relying on a high fidelity database and *a posteriori* demonstrations as full CFD of a flow problem, converging from some initial condition. Uncertainty quantification, therefore, aims to understand why certain models fail and model development attempts to correct such deficiencies. A priori relates to the assumption that machine-learning approaches successfully minimising some objective on high-fidelity data, a process known as training, will improve CFD performance. A posteriori aims to demonstrate this reasoning and is consequently much harder to establish, yet vital for successful industrial implementation.

In efforts to understand uncertainty, databases can be inspected and used as a road-map (Hunt and Savill, 2005; Schmitt, 2007), to give the engineer an idea of whether a given closure is applicable for a given flow topology. More complex machine-learning approaches have had their ability to identify regions of inaccuracy assessed (Ling and Templeton, 2015). Presenting another method of general uncertainty identification, Spalart et al. (2015) have passively solved the RANS equations using a DNS mean flow to assess closure quality. Edeling et al. (2014b) used Bayesian methods for identifying the uncertainty in the values of closure coefficients, whilst Xiao et al. (2016) applied similar methods for quantifying uncertainty in predicted flow quantities.

In terms of model development, the eddy viscosity has been optimised to find the β^* coefficient in the $k - \omega$ -SST turbulence model that best applies to a turbomachinery flow (Weatheritt et al., 2017b). This was done using least-squares regression in an *a priori* manner that has been previously applied many times (Muldoon and Acharya, 2006; Spalart et al., 2015; Pichler et al., 2015). Correction parameters have been learnt and added to the model transport equations by Parish and Duraisamy (2016); however, these were a function of space, limiting any *a posteriori* demonstration to an identical geometry. Such studies have elicited the argument to ensure Galilean invariance in machine-learning approaches and, when adhered to, the resulting model performs better (Ling et al., 2016). Edeling et al. (2014a) have used Bayesian methods to modify model coefficients for a full *a posteriori* demonstration. This is encouraging, yet proved to be a computationally intensive approach.

More complex regression methods, that alter more than the coefficients in the original model are possible (say adding new non-linear

terms). For example, neural networks (e.g. LeCun et al., 2015) have been used to replace terms in the RANS equations. Ling et al. (2016) used deep neural networks to model the Reynolds stress and whilst showing good *a priori* agreement, the only *a posteriori* demonstration required the matrix of Reynolds stresses at each grid point to be inserted into the solver — thus limiting the model to the same flow geometry. Because of this apparent difficulty at full CFD implementation, a neural network has been used to correct a converged linear RANS solution (Weatheritt et al., 2017a) in a similar fashion to random forest regression (Ling et al., 2017). The primary issue with this approach is, that should the linear RANS model predict a vastly inaccurate flow field, as with the present study, then the modified Reynolds stresses are still a function of the incorrect velocity field. In other words, the method is unable to alter global phenomena such as separation and reattachment points, for example.

Another emerging approach to model development is via symbolic regression, which most commonly manifests itself as a variant of genetic programming (Koza, 1992). Symbolic regression aims to return a mathematical equation that best fits some high-fidelity data, both in terms of error and simplicity. No model is provided as a starting point by the user and the algorithm searches the space of all mathematical expressions. This has several advantages over other machine-learning techniques. Primarily, the resulting equation is tangible and can be implemented into a CFD code readily. Genetic programming is an evolutionary algorithm (e.g. Steeb, 2014), which evolves a collection of candidate solutions analogous to Darwin's (1858) theory of natural selection. Such approaches have been applied to separated flow (Weatheritt and Sandberg, 2016c); a modified version of the original gene expression programming (GEP) concept of Ferreira (2001), suitable for tensor regression, showed excellent skin friction prediction in *a posteriori* demonstrations. This was achieved by optimising a non-linear stress-strain relationship. However, the modelled time scale was not correctly accounted for during the machine-learning phase³ and the objective function did not account for the magnitude of the modelled Reynolds stress. Further studies for RANS modelling have performed well in *a priori* studies (Weatheritt et al., 2017a; 2017b). Note, the framework is also being developed for hybrid RANS/LES methods (Weatheritt and Sandberg, 2015; 2016a; 2016b).

In this work, we present an extension of our GEP evolutionary framework to account for the proper modelling of the turbulent time scale and new objective function to account for the magnitude of the Reynolds stress. We develop this framework with the following considerations:

1. Resulting models are easy to implement into CFD codes.
2. Resulting models are Galilean invariant.
3. Demonstrate *a priori* success on flows similar to the high-fidelity training database.
4. Demonstrate *a posteriori* success on complex flows, by solving all transport equations from an initial condition. Hence validating exactly as a conventional turbulence model would be.
5. The entire framework is computationally feasible for industrial application.

By ensuring these points, this paper presents a major contribution to the field of machine-learning for turbulence modelling. Above, we identified the linear stress-strain relationship as a major contributor to uncertainty and so we target this for improvement, effectively producing an EASM. We apply our framework to duct flows, using hybrid RANS/LES (H-R/L) data to build new stress-strain equations. The algorithm is non-deterministic, meaning for each database we produce a class of unique models and then gain statistical information regarding algorithm performance. The use of H-R/L shows that high-resolution

³ Although the authors argued this was unnecessary.

DNS or even LES is not necessarily required for machine-learning. These are then tested *a priori* on similar yet different ducts and then *a posteriori* on a further, wide aspect ratio duct and an asymmetric diffuser. Both of these *a posteriori* cases are examples where a linear model completely fails to predict the velocity field globally. This two stage validation process presents one of the most intensive validation processes of machine learnt turbulence models to date and demonstrates that the evolved models can be stable in a flow configuration vastly different from their training regime.

This paper is structured as follows. Section 2 outlines the RANS framework we adopt, in particular, the target for improvement and implementation into a CFD code. Section 3 briefly discusses the hybrid methodology used to build the high-fidelity data. Information on the test cases used for training and testing the new models is contained in Section 4. Section 5 introduces our evolutionary framework, including our handling of the high-fidelity data and new objective function. The results from the machine-learning algorithm, including *a priori* demonstration is found in Section 6 and *a posteriori* CFD results in Section 7. Finally, our conclusions are drawn in Section 8.

2. RANS framework

A key part of most turbulence closures is the linear stress-strain relationship, known as the Boussinesq approximation,

$$a_{ij} \equiv \frac{\tau_{ij}}{2k} - \frac{1}{3}\delta_{ij} \quad (\text{def.}) \quad (1a)$$

$$a_{ij} = -\tau_l S_{ij} \quad (\text{linear}) \quad (1b)$$

$$a_{ij} = a_{ij}(V_{ij}^1, V_{ij}^2, \dots, I_1, I_2, \dots) \quad (\text{EASM}) \quad (1c)$$

$$= -\tau_l S_{ij} + a_{ij}^x(V_{ij}^1, V_{ij}^2, \dots, I_1, I_2, \dots) \quad (1d)$$

which relates the anisotropy a_{ij} of the Reynolds stress $\tau_{ij} = \overline{u'_i u'_j}$ to mean strain rates $S_{ij} = \frac{1}{2}(\partial_{xy} U_i + \partial_{xz} U_j)$ (Eq. 1b). τ_l is the turbulent time scale from the RANS model and $k = \frac{1}{2}\tau_{ii}$ is the turbulent kinetic energy. EASMs begin from the weak equilibrium hypothesis (Rodi, 1976) to write down non-linear terms in $\partial_{xy} U_i$ for the anisotropy tensor. V_{ij}^k and I_k in Eq. (1c) are functions of S_{ij} and $\Omega_{ij} = \frac{1}{2}(\partial_{xy} U_i - \partial_{xz} U_j)$. Further, by defining $s_{ij} = \tau_l S_{ij}$ and $w_{ij} = \tau_l \Omega_{ij}$, V_{ij}^k is an integrity basis for a_{ij} and I_k are invariants from the Cayley–Hamilton theorem (Pope, 1975),

$$\begin{aligned} V_{ij}^1 &= s_{ij}, \quad V_{ij}^2 = s_{ik} w_{kj} - w_{ik} s_{kj}, \\ V_{ij}^3 &= s_{ik} s_{kj} - \frac{1}{3}\delta_{ij} s_{mn} s_{nm}, \\ &\vdots \\ I_1 &= s_{mn} s_{nm}, \quad I_2 = w_{mn} w_{nm}, \dots \end{aligned} \quad (2)$$

An EASM aims to close Eq. (1c) by writing down algebraic expressions of variables from Eq. (2); we recall our examples from Section 1 of Gatski and Speziale (1993), Wallin and Johansson (2000) and Craft et al. (2000).

The integrity basis is vital for ensuring Galilean invariance (Spencer and Rivlin, 1958; 1959). a_{ij} is a symmetric, traceless tensor and the space of such tensors functionally dependent on s_{ij} and w_{ij} is spanned by V_{ij}^k , $k \leq 10$, ensuring invariance under group transformation. Note these are still linearly independent in the same manner that monomials in x are spanned by the basis $\{x^p | p \in \mathbb{N}\}$. In this work, however, we limit ourselves to the three shown in Eq. (2). Further note, there are five invariants — but again we limit ourselves to I_1 and I_2 . This is because Weinmann and Sandberg (2009) found there to be limited gains in predictive accuracy from three-dimensional EASM formulations applied to complex geometries and upon assuming two-dimensionality, the required basis reduces to three and the independent invariants to two. This also is likely to assist with numerical stiffness: $V_{ij}^{5,6}$ are cubic in $\partial_{xy} U_i, V_{ij}^{7-9}$ are quartic, V_{ij}^{10} is quintic and the not included dependent

scalar invariants are at least cubic. By not including these terms, the dependency on higher order gradients is reduced, thus alleviating potential issues on non-orthogonal/unstructured/skewed grids.

Eq. (1d) decomposes the anisotropy into the standard linear relation and an extra anisotropy tensor a_{ij}^x . Note that $a_{ij}^x = a_{ij}^x(V_{ij}^1, \dots)$ and so functionally, Eq. (1c) is identical to Eq. (1d). In this study, we optimise a stress-strain relationship by obtaining the a_{ij}^x that best approximates our high-fidelity duct database. That is, we give our equations for anisotropy the standard linear part “for free.” This is important in code implementation for several reasons. Most transport equations in current turbulence models are developed intending this term. Therefore, should the algorithm not find this term (or something similar), then the numerical stability of the overall turbulence model is drastically impacted.⁴ Secondly, some turbulence codes may not offer the user much freedom in model manipulation: it may not be trivial to remove this term from the transport equations. Finally, for optimal numerical stability, a mixture of implicit and explicit treatment of terms is required. For example, we have used the open source code OpenFOAM (Weller et al., 1998) for this work, which allows for the implicit treatment of part of the effective momentum diffusion,

$$\underbrace{-\partial_{xy}(\nu_t + \nu)\partial_{xy} U_i}_{\text{implicit part of molecular and linear turbulent diffusion}} - \underbrace{\partial_{xy}(\nu_t + \nu)\partial_{xi} U_j}_{\text{explicit part of molecular and linear turbulent diffusion}} + \underbrace{2\partial_{xy} k a_{ij}^x}_{\text{explicit extra anisotropy}}, \quad (3)$$

where the term $2k/3$ has been absorbed into the (modified) pressure p/ρ . We implement this effective diffusion into the incompressible $k - \omega$ -SST turbulence model (Menter, 1994). As well as the momentum equation, a_{ij}^x also appears in the production of turbulent kinetic energy,

$$P_k = 2\nu_t S_{ij} S_{ij} - 2ka_{ij}^x S_{ij}. \quad (4)$$

The implementation of this term is discussed in Section 6.4. The final terms where a_{ij}^x can impact the equations are gradient diffusion models for k and ω . However, at this stage, we do not implement the generalised gradient diffusion hypothesis of Daly and Harlow (1970), in the same manner as Wallin and Johansson (2000). Therefore, we retain the standard linear gradient diffusion hypothesis.

In summary, the evolutionary algorithm, introduced in Section 5, is tasked with finding an expression for a_{ij}^x of the form Eq. (1d), that sits in the expression,

$$\tau_{ij} = \frac{2}{3}k\delta_{ij} - 2\nu_t S_{ij} + 2ka_{ij}^x, \quad (5)$$

where,

$$a_{ij}^x = \beta_1(I_1, I_2)V_{ij}^1 + \beta_2(I_1, I_2)V_{ij}^2 + \beta_3(I_1, I_2)V_{ij}^3. \quad (6)$$

The challenge for the machine-learning is thus to find $\beta_k = \beta_k(I_1, I_2)$. We have outlined our specific implementation into the SST model, yet this is not a requirement — one is free to use their own baseline model.

3. Hybrid framework

Most current machine-learning frameworks that model develop via regression rely heavily on a high-fidelity LES (e.g. Weatheritt et al., 2017a; Ling et al., 2017) or even DNS (Weatheritt and Sandberg, 2016c). Yet, for RANS model development the only requirements are statistical profiles. Therefore, perhaps in current studies, there is surplus compute power. In this paper, we use statistics from a H-R/L database, which can be obtained at a fraction of the cost. This is a vital exercise for industrial application; often the Reynolds numbers of interest exceed that currently feasible with higher fidelity methods (Hanjalić, 2005). Even though H-R/L will not provide a perfect

⁴ This was confirmed through early tests of the framework (Weatheritt and Sandberg, 2016c).

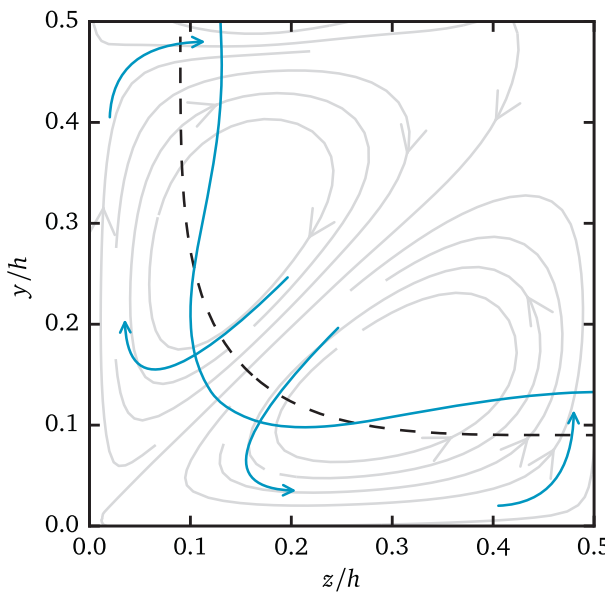


Fig. 1. The effect of mean secondary vortices (MSVs) on streamwise velocity. Flow is into the page, solid boundaries exist on the axes. (—) mean streamwise velocity contour $U = U_b$ for turbulent flow, (---) laminar flow schematic, (→) MSV, (—) cross plane streamlines. Data is from H-R/L of the VIN1 case.

replacement to a DNS, LES or experiment, we feel that the H-R/L data is reasonable for our purposes. [The GEP methodology, introduced in Section 5, only requires a list of stress values, basis functions and invariants \(Eq. \(2\)\)](#). This is independent of the coordinates x , y and z . In other words, provided that locally the H-R/L provides representative values of stress for a given velocity gradient tensor, a reasonable RANS model may be expected. That said, we cannot hope to improve upon global inaccuracies caused by misreporting the stress for a given velocity gradient in the H-R/L flow field. Note, we do not recommend H-R/L as best practice; we are merely showing the feasibility of such a workflow. We have used DNS data in a previous study to good effect ([Weatheritt and Sandberg, 2016c](#)).

We use our in-house H-R/L approach ([Weatheritt and Sandberg, 2017](#)), which is an iteration of [Weinmann et al.'s \(2014\)](#) Flow Simulation Methodology (FSM). We employ a continuous blending function f which is bound between 1 (RANS) and 0 (DNS). In this sense, the methodology is classified as a unified approach ([Fröhlich and von Terzi, 2008](#)) similar to Detached Eddy Simulation ([Spalart, 2009](#)).

4. Flow configurations

Internal flow, in particular through a rectangular cross-section, is prevalent in automotive, aeronautic, medical and infrastructural disciplines. The finite extent of the streamwise normal plane provides a modelling challenge, particularly in the corners. Mean secondary vortices (MSV) ([Fig. 1](#)) are observed, originating from these corners. Whilst small in magnitude, they exert a large effect on global flow features ([von Terzi et al., 2011](#)). They act to deflect the velocity towards the centre of the duct, pinching the corners of the flow field, which can mix sediment from the walls into the bulk and affect downstream separation in subsequent geometrical asymmetries (See [Section 4.3](#)).

Such secondary motions are Reynolds stress induced (e.g. [Moinuddin et al., 2004](#)). Their absence when predictions are made with linear closures is easily understood from the Reynolds-averaged

streamwise vorticity equation. The substitution of [Eq. \(1b\)](#) into the source term $-\varepsilon_{ijk}\partial_{x_j}\partial_{x_m}\tau_{km}$ yields,⁵

$$\begin{aligned} (\partial_{x_3}^2 - \partial_{x_2}^2)(\tau_{23}) + \partial_{x_2}\partial_{x_3}(\tau_{22} - \tau_{33}) = \\ (\partial_{x_2}^2 - \partial_{x_3}^2)(\nu_t(\partial_{x_3}U_2 + \partial_{x_2}U_3)) + \\ 2\partial_{x_2}\partial_{x_3}(\nu_t(\partial_{x_3}U_3 - \partial_{x_2}U_2)) = 0. \end{aligned} \quad (7)$$

Since there is zero redistribution of streamwise momentum, this trivially holds. Consequently, secondary motion is not observed when using linear closures. [Fig. 2](#) shows the lack of mean streamwise velocity distortion, a direct result of the MSVs. This qualitative failure to predict even first order statistics, by the industry standard, makes these types of geometries perfect for consideration in this paper. That is, we demonstrate the possible benefit of a relatively hands-off method to improve predictions for a given class of flow.

4.1. Testing regime

We use a series of internal flows to produce our new anisotropy models a_{ij}^x , capable of resolving MSVs. [Table 1](#) details the cases used, which are introduced in the following sections. The “use” column dictates how each case is implicated in the process. “T” denotes a training case (and *a priori* validation) and “V” denotes a RANS validation case. Therefore T cases form the training database (used to create models) for which a H-R/L simulation is required, but V cases only require a RANS setup. Currently, we keep the training cases separate, implying two distinct high-fidelity databases and thus two new classes of model. These classes will be discussed throughout this paper. Each class is named after its associated data set. [Fig. 3](#) outlines the testing regime we have adopted. The divide separates the cases into training databases (left) and testing cases (right). Note that we also use the training databases for *a priori* validation.

For *a priori* validation, a model of the form [Eq. \(6\)](#), is applied to the high-fidelity databases VIN1 and CHY33. This means that V_{ij}^k and I_k are calculated using the true velocity gradients. This model is then compared against the true Reynolds stress. See [Section 5](#) on how the modelled k and ω are calculated. For *a posteriori* validation, a model of the form is implemented as described in [Section 2](#) into OpenFOAM. The cases VIN1, CHY33, VIN7 and DIFF are then solved from the initial condition $U = 0$, $k = 0$, etc, until a steady state is obtained. The following sections now introduce the cases used throughout this methodology.

In total, 15 models from each H-R/L database are constructed. Those from the CHY33 case are denoted C1-15 and similarly for the VIN1 case the models are labelled V1-15. Further, we can ensemble these models into two average models, these are labelled \tilde{C} and \tilde{V} . Note, each set of models is colour coded, C models are red and V models are blue in subsequent plots.

4.2. Ducts

Ducts are amongst the simplest internal flows that present MSVs. As discussed above, the linear Boussinesq model entirely fails to predict such secondary motion (see [Eq. \(7\)](#) and [Fig. 2](#)). Therefore, this type of flow is a perfect example of how we can utilise the evolutionary methodology, presented in [Section 5](#), to produce an improved Reynolds stress model.

There are numerous duct studies in the literature (e.g. [Gessner, 1973](#); [Huser and Biringen, 1992](#); [Uhlmann et al., 2007](#)) and we have outlined the duct cases VIN1, VIN7 ([Vinuesa et al., 2014](#)) and CHY33 ([Cherry et al., 2008](#)). The first two are DNS; an equal aspect ratio (AR) duct and an aspect ratio 7 duct respectively. The latter is an experiment of an aspect ratio 3.3 duct, which in the original paper served as an inflow to an asymmetric diffuser, discussed in [Section 4.3](#).

⁵ taking $x = x_1$ as the streamwise direction.

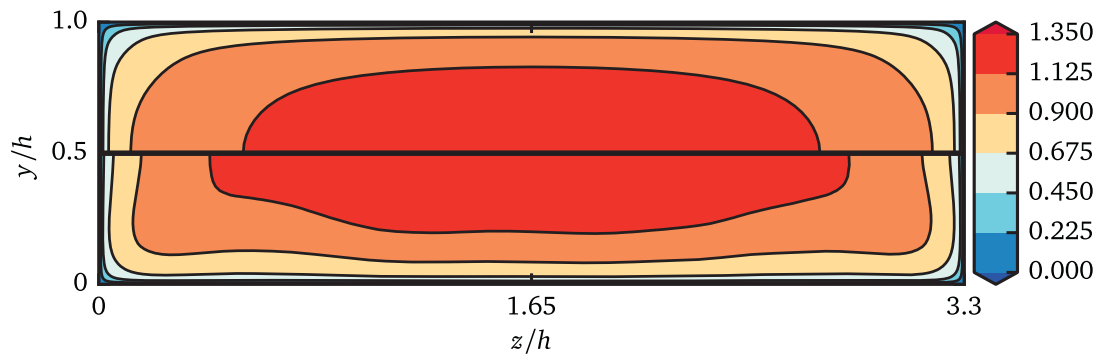


Fig. 2. Streamwise velocity for the CHY33 case (see Table 1). Top: Linear $k - \omega$ -SST. Bottom: H-R/L.

Table 1
Cases considered.

case	DNS* / exp **	Re_b	AR	use
CHY33	Cherry et al. (2008)**	10,000	3.3	T,V
DIFF			3.3 → 1	V
VIN1	Vinuesa et al. (2014)*	10,000	1	T,V
VIN7		5000	7	V

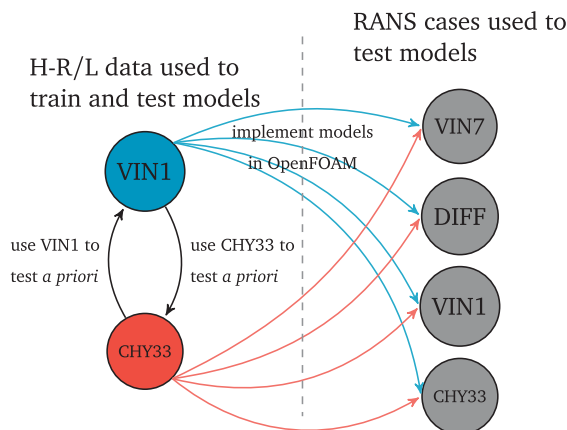


Fig. 3. Testing schedule.

Note, the training cases, VIN1 and CHY33 are “easier” than the VIN test case. This is because there is a greater deal of asymmetry in the flow.

4.2.1. VIN1

This case was initially part of a DNS study by Vinuesa et al. (2014) exploring different aspect ratios. VIN1 is of equal aspect ratio ($AR = 1$) and the Reynolds number based on bulk velocity U_b and channel height h (see Fig. 4) is $Re_b = 10,000$.

The H-R/L was solved using 25,000 cells in the $y - z$ plane and 200 for the periodic streamwise direction of $6h$, ensuring a y^+ less than one for all walls. Fig. 5 shows the resolved structures through the $-\lambda_2$ criterion, where one observes the “detached-eddy” nature of the method. See Fig. 6 for a comparison with the original DNS case. The overall flow topology is reasonably predicted, but the MSVs are too far from the wall and there is a general over pinching of the bulk flow.

For the RANS, we used only a quarter of the domain and applied symmetry along the centre lines (See Fig. 7). We solve in a $y - z$ plane of 1024 cells, ensuring $y^+ < 1$. Note, we tested that the symmetric boundary conditions didn’t “help” the flow converge, by solving the full domain using one of our trained non-linear models.

4.2.2. CHY33

This duct has an aspect ratio $AR = 3.3$, see Fig. 4, forming the inflow to the diffuser of Section 4.3, originally experimentally studied by Cherry et al. (2008) and more recently solved using DNS (Ohlsson et al., 2010). To build the training database, the H-R/L grid contained 14,400 cells in the spanwise plane and 145 in the periodic streamwise direction. As with VIN1, this was $6h$ in length (h being the length of the smaller side). This is quite a coarse grid over a small domain, for this $Re_b = 10,000$ flow,⁶ but the point of the exercise is to demonstrate cost saving to the extent that practicality for industrial applications can be argued.

Fig. 8 compares the H-R/L with the DNS (Ohlsson et al., 2010). Note that the comparison is not perfect as the DNS is taken from their diffuser study at $x = -2h$, where it is likely the pressure gradient induced from the expansion is felt. Despite this slight inconsistency in the comparisons, the H-R/L is seen to give a good idea of the streamwise velocity U/U_b — see also Fig. 2 for the $y - z$ plane, which shows the correct qualitative flow field. The turbulent kinetic energy, however, is not perfect near the wall — the H-R/L misses the inner peak maximum. This is a consequence of the coarse mesh and therefore the slow formation of turbulent structures.

The RANS test cases are solved in a quarter of the domain, as described in Section 4.2.1, testing beforehand that the imposed symmetry on the flow did not assist the non-linear models’ convergence. The total grid count in the $y - z$ plane was 5,500.

4.2.3. VIN7

This case is the first reported that does not form part of the training database, see Table 1 and Fig. 3, so there is no H-R/L setup required. It initially was part of the same study as VIN1 and at $AR = 7$, was the maximal aspect ratio considered (Vinuesa et al., 2014). Despite the Reynolds number $Re_b = 5,000$ being half that of VIN1, due to the geometrical asymmetry, the model must correctly predict the larger difference between τ_{22} and τ_{33} (see the top line of Eq. 7). This implies an increase in difficulty over the training databases. We can see the effect of both Reynolds number and aspect ratio on the cross sectional shape, seen in Fig. 4 relative to VIN1 and CHY33.

The RANS simulation, as with VIN1 and CHY33, solves for one quarter of the physical domain using a total of 7000 points, ensuring $y^+ < 1$.

4.3. Diffuser

The asymmetric diffuser (Cherry et al., 2008; Ohlsson et al., 2010), described geometrically in Fig. 4, has become a classic case for turbulence model validation. As already mentioned in the discussion surrounding Eq. (7), the linear model fails to predict the presence of MSVs,

⁶ Cherry et al. (2008) defines the Reynolds number with half channel height, so reports a value of 5,000.

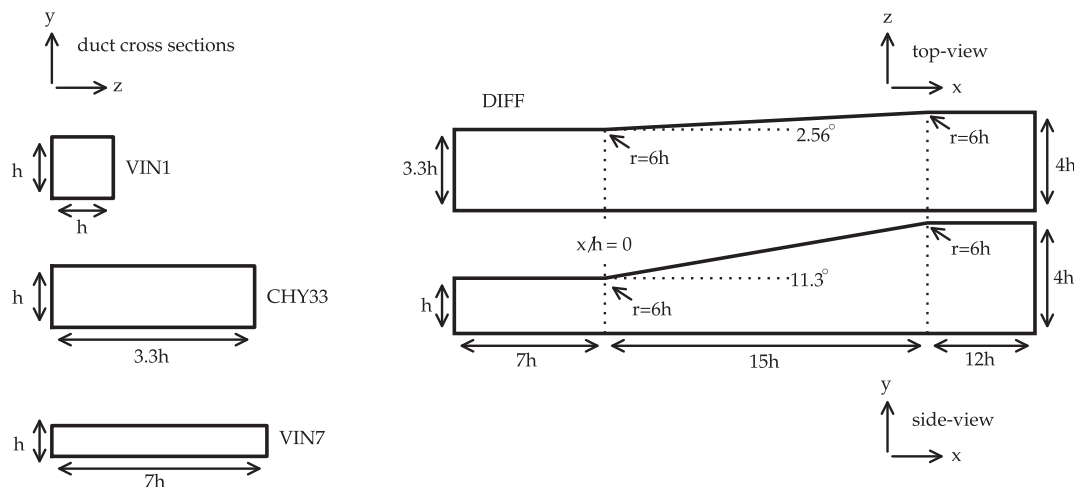


Fig. 4. Geometries of cases considered. In all flows, x is the streamwise direction. See Table 1 for reference. The duct cross sections are scaled such that U_b and ν are the same in all cases. For the diffuser, each corner is smoothed into an arc with radius $6h$.

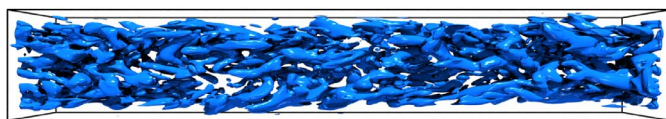


Fig. 5. H-R/L, VIN1, $-\lambda_2 = U_0^2/h^2$. Flow is from left to right.

which impacts on the results for this diffuser. Fig. 9 shows contours of streamwise velocity, with the line $U = 0$ highlighted in red. A combination of no MSVs in the flow (von Terzi et al., 2011) and then subsequent errors in $\tau_{33} - \tau_{22}$ and τ_{23} (being functions of strain only), the flow separates from the wrong side of the diffuser. Consequently, this flow (and similar topologies) have been the target of EASM/full Reynolds-stress Models (RSM) models (Abe et al., 2003; Gullman-Strand et al., 2004; Steiner et al., 2009; Jakirlić et al., 2010; Menter et al., 2012). In all cases, EASMs out performed linear models, yet for the diffuser studied here the conclusion of an ATAAC investigation (Schütze et al., 2012) was that EASMs/RSMs, “give reasonable agreement of the predicted flow topology with the experiment, but the results scatter considerably with different models.” From this workshop the best result came from an elliptic-blending RSM approach, which solves a total of 8 transport equations for the turbulence, making it computationally more intensive than the 2-equation models used here.

This case is for validation only, so we require just a RANS setup. For this we used a structured mesh consisting of 1.8×10^6 cells. This includes a development section of $7h$, which contains a $2h$ recycling region, the expansion region is $15h$ which is followed by a downstream region of $12h$. The wall resolution is such that $y^+ < 1$. For a complete description of the geometry see Fig. 4. The CHY33 duct serves as the inlet, therefore the Reynolds number based on h at the inlet is the same as above at $Re_b = 10,000$.

5. Evolutionary methodology

A regression needs input (independent) and output (dependent) variables. Further, one must have the expected (target) value of the output for given values of the inputs. From such a data set, we can fit a model, the output of our framework. Fig. 10 provides a road-map for the preparation of the inputs and target required to obtain our desired output. We assume that the a_{ij} obtained from the hybrid simulations is close to the ‘true’ value. The RANS equations do not provide us with the true (specific) dissipation rate because the ω and ϵ equations are largely empirical and tweaked in order to return a good shear stress prediction in attached boundary layers. This means that the time scale from a scale

resolving simulation is not representative of the time scale of our RANS system of equations. Further, the dissipation rate is notoriously tricky to calculate, especially if the simulation contains a subgrid model. Instead, one may extract the dissipation rate via a frozen/pассив solving of the turbulent transport equations (Parneix et al., 1998). This freezes the mean velocity and Reynolds stress obtained from the hybrid simulation and then by solving only for ω , one obtains the ‘correctly modelled’ turbulent time scale $\tau_t = 1/\omega$ given the true velocity and turbulent stress. From U , k and ω one can compute Eq. (2), which serves as the input. The target variable a_{ij}^x is similarly calculated, using the true velocity gradient, Reynolds stress and modelled time scale.

The regression is done *symbolically*, that is new models are tangible mathematical equations in V_{ij}^k and I_k . The work presented here is an extension to the framework detailed by Weatheritt and Sandberg (2016c). Evolutionary algorithms, that mimic nature’s survival of the fittest — by iterating non-deterministically to optimise a problem, brought symbolic regression into the computer domain.

For example, an algebraic expression of the form Eq. (1d),

$$a_{ij}^x = V_{ij}^1 - (V_{ij}^3 + (I_1 \sqrt{I_2} V_{ij}^2)) \quad (8)$$

is written in what is called expression tree (ET) form in Fig. 11. In GEP such ETs are constructed from chromosomes,

$$- V_1 + V_3 p | V_2 V_3 V_2 V_3 V_2 V_1$$

$$* I_1 Q | I_2 I_1 I_2 I_2$$

The chromosomes are read left to right, with each representing a tree in Fig. 11. The $|$ denotes a split between head and tail of the chromosome and the Q is the square root. The head may consist of operators and variables and the tail only of variables. By ensuring the tail contains one more symbol than the head, mathematical syntax is guaranteed. This means that not all symbols are ‘expressed’ in the final equation. The reader is pointed to Ferreira (2001) for more details. These trees are read recursively in order to reconstruct Eq. (8). The p symbol, introduced and named the plasmid by Weatheritt and Sandberg (2016c), is a symbiotic join between the two chromosomes. The first is a tensor expression and the second is a scalar field. The introduction of the plasmid has made it possible to regress variables that are not all of the same dimension. For a full discussion see Weatheritt and Sandberg (2016c).

A population of such chromosomes are randomly generated, then evolved according to survival of the fittest. During each successive generation, expressions that better approximate the target values are more likely to mate and provide genetic material to the next generation. Further, mutation is mimicked by randomly introducing errors. For full details see Ferreira (2001). Once a stopping criterion has been met,

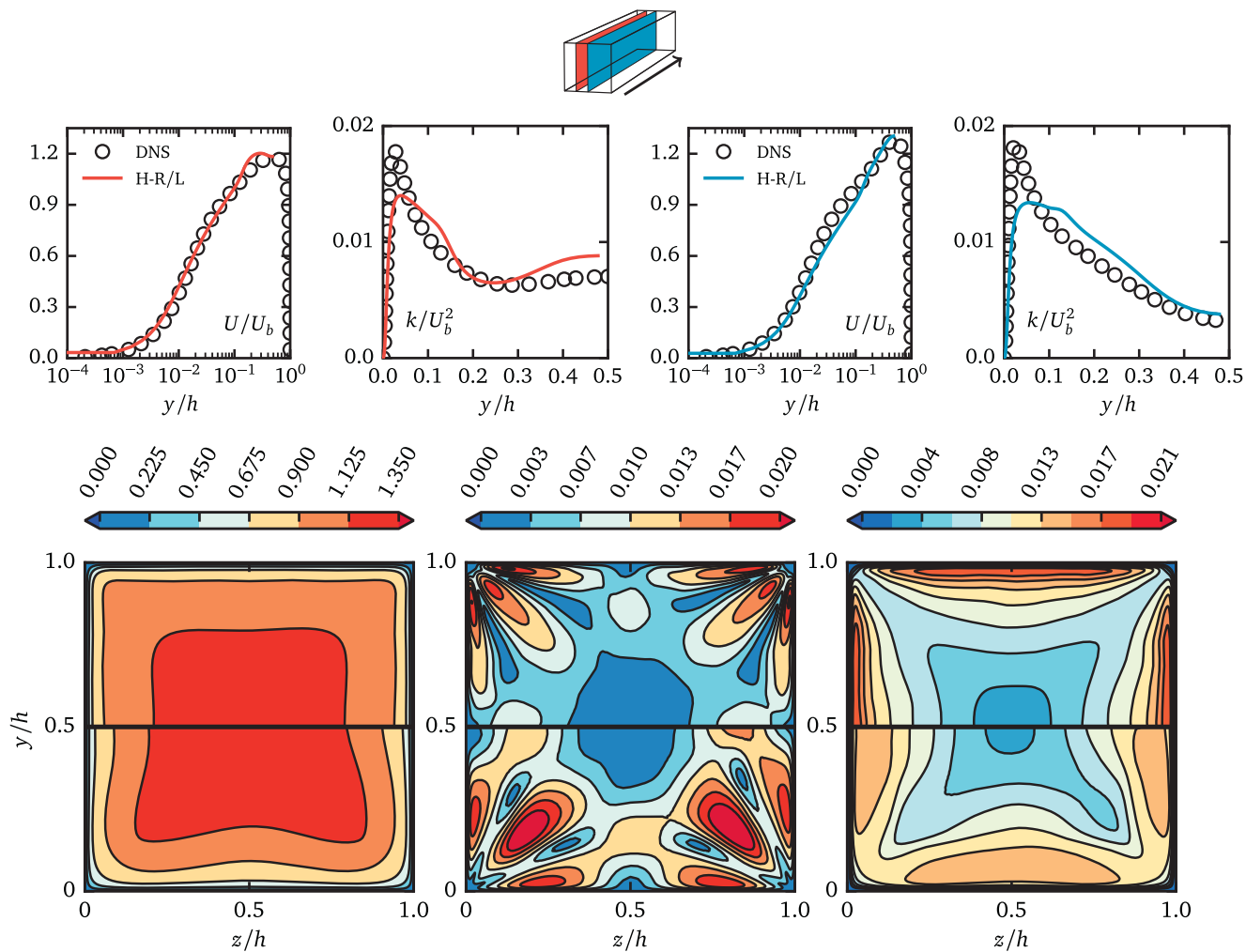


Fig. 6. H-R/L compared to the VIN1 DNS (Vinuesa et al., 2014) at $z = \frac{1}{4}h, \frac{1}{2}h$. The H-R/L results are averaged in the time and streamwise directions (see schematic, arrow shows streamwise direction). Contours (L-R): U/U_b , $\sqrt{V^2 + W^2}/U_b$, k/U_b^2 . Top half: DNS, bottom half: H-R/L.

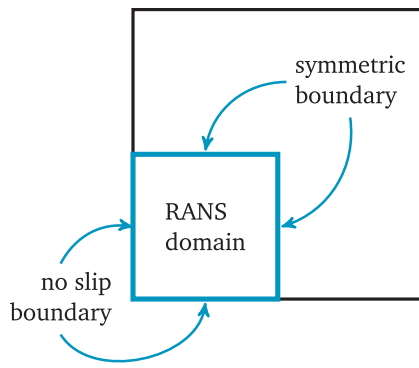


Fig. 7. RANS solution domain for the VIN1 case. Flow is into the page.

which is usually a finite number of generations, the best expression from the population is taken as the output.

The fitness, or cost, of an expression is calculated as the distance from the training data,

$$\text{Fit}(a_{ij}^{x \text{ guess}}) = \frac{1}{6N} \sum_k^N \sum_i^3 \sum_{j=1}^{j \leq i} |a_{ij}^{x \text{ guess}}(x_k) - a_{ij}^x(x_k)|. \quad (9)$$

$|\cdot|$ is the absolute value and the summation is over the N training data points x_k . The original implementation of our framework used the double inner product which measures the alignment of $a_{ij}^{x \text{ guess}}$ and a_{ij}^x ,

however this was found to produce solutions of the wrong magnitude. Here we test Eq. 9 as the sole objective. Future optimisations may simultaneously maximise alignment and magnitude objectives.

Two sets of H-R/L training data are available. Two-dimensional planes consisting of approximately 6000 and 3500 training points are used for the VIN1 and CHY33 cases respectively. This is a significant increase over the pilot study (Weatheritt and Sandberg, 2016c). Training time, set to 1500 generations, of a population of 200 individuals is on the order of one core hour.

6. Model training and *a priori* validation

6.1. The evolutionary process

From each of the thirty runs of the algorithm, the best member of the population (that which minimises Eq. (9)) after the last generation $i = 1500$ is taken as our model. The mean best member of each population as a function of generation is plotted in Fig. 12, along with a 95% confidence interval for this mean. The evolutionary runs that produced C1 and V1 are shown alongside. This second plot shows not only the best member of the population, but also the mean of the entire population that spawned C1 and V1. Clearly, as previously hypothesised, the anisotropy in the VIN1 case is easier to minimise, due to the higher level of symmetry, yet the models V1-15 contain a much higher variation in fitness than C1-15. From the C1 and V1 transient, one observes step changes in fitness much like Darwin (1858) hypothesised

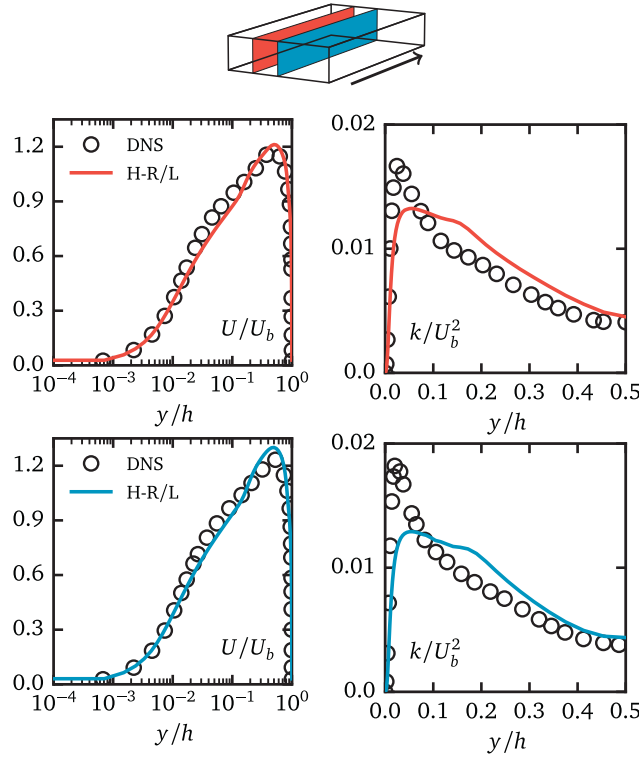


Fig. 8. CHY33 H-R/L compared to the DIFF DNS (Ohlsson et al., 2010) at $z = \frac{1}{4}h, \frac{1}{2}h$. The H-R/L results are averaged in the time and streamwise directions (see schematic, arrow shows streamwise direction).

for biological evolution, not a gradual improvement each generation. These step changes are the rare event a mutation in an individual is beneficial and is then better than the current minimum. In contrast, we see no long term change in the population average as individual fitness scores fluctuate.

From the left-hand side plots of mean best fitness, we see that the majority of improvement is found in early generations. This is to be expected, as the initial population is randomly created. That said, we see the population is not entirely converged at $i = 1500$ and consequently should we run the algorithm longer, then we could expect further improvements to fitness.

6.2. An inspection of the model equations and deduction of MSV dynamics

One of the main advantages of GEP, and symbolic regression in general, is the ability to observe the functional relationship produced. By the very nature that the algorithm is symbolic, we obtain a mathematical expression. For example, the fittest individual in V1-15 is V6, given by the equation

$$\begin{aligned} a_{ij}^x = & 2V_{ij}^1(I_1 - I_2) \\ & - V_{ij}^2(I_1 - I_2 + 1/\exp(3I_2 + \exp(-I_1)\log(I_1 - 2I_2))) \\ & + \log(I_2) + V_{ij}^3(I_2 + (1/\exp(3I_1 - 1))^2). \end{aligned} \quad (10)$$

This equation is highly non-linear and we might surmise that this in a CFD solver might cause numerical stiffness, due to the nested transcendental functions. Note that the complexity of symbolic regression expressions can be monitored (Le et al., 2016), but we do not currently implement such checks. However, as shall be shown, the GEP algorithm rarely produced a function that could not be used successfully within OpenFOAM, which is a finding consistent with an earlier study (Weatheritt and Sandberg, 2016c). Instead, consider the equation for V13, the second best model of the V1-15 class, is

$$\begin{aligned} a_{ij}^x = & 2I_1V_{ij}^1(4I_1 - 2I_2 + (I_1 - I_2)^2 + 2) \\ & + V_{ij}^2(2.95I_1 - 0.59 - \log(I_1))\log(I_1) \\ & + V_{ij}^3(2 - \log(I_1(2I_1 - I_2)(\exp(-I_2) + 2))). \end{aligned} \quad (11)$$

This equation is, despite being non-linear, much more amicable to discretisation. We will return to this in Section 7.

We can analyse the produced equations for a_{ij}^x by looking at all equation fragments. Practically, this involves treating each equation as a tree (like Fig. 11) and recording all its subtrees. As we have a total of only 30 models, C1-15 and V1-15 are treated together. Firstly of note, in the V_{ij}^2 and V_{ij}^3 components, \log has been used a total of 29 times with the scalar invariants I_1 and I_2 . $\log(I_1)$ occurs 20 times, whilst $\log|I_2|$ appears 9. This shows that the logarithm has been used on average almost every time in the production of the best solution. That said, there are no common equation fragments of any great length appearing as coefficients for V_{ij}^2 and V_{ij}^3 . The longest repeating fragment is $4I_1^3I_2V_{ij}^2$, which has been used twice. This means that starting from two different initial conditions, the optimisation process has independently produced this expression.

The story is much different for the V_{ij}^1 coefficient, a total of six times (i.e. 20%) the entire V_{ij}^1 term, under simplification,⁷ was found to be

$$2(I_1 - I_2)V_{ij}^1. \quad (12)$$

Take for example Eq. (10). Twice further this term was

$$(I_1 + 5I_2^2 - 3I_2)V_{ij}^1. \quad (13)$$

This shows that the algorithm is capable of finding a functional relationship for this term. On the flip side, it appears that for the V_{ij}^2 and V_{ij}^3 terms, there is no coherent functional form and the algorithm has found many ways to minimise Eq. (9). This is particularly interesting for this case; despite a coherent picture in V_{ij}^1 , this term is not responsible for creating MSVs — there is no dependence on $\partial_x U$ — but it is responsible for maintaining these secondary flow structures. Consider that Eq. (12) implies a relationship,

$$a_{ij} = \underbrace{4\tau_I^3 Q S_{ij}}_{\text{MSVdetection}} + \underbrace{(2\tau_I^3 S^2 - \tau_I)S_{ij}}_{\text{lineardampingunderstrain}} + \underbrace{\sum_{k>1} \beta_k V_{ij}^k}_{\text{non-linearterm}}, \quad (14)$$

of proportionality of stress and strain via the Q vortex criterion (Hunt et al., 1988; Haller, 2005) where the quantity Q is defined,

$$Q = \frac{1}{2}(\Omega_{ij}\Omega_{ij} - S_{ij}S_{ij}). \quad (15)$$

The second linear term has absorbed the standard Boussinesq approximation and implies redistribution in straining flows. When $Q < 0$, the proportionality of stress and strain is still positive. In other words, this acts to damp the eddy viscosity in strain dominated flow. Note, the dynamics described by Eq. (14) have been previously seen in a mathematically derived EASM of Apsley and Leschziner (1998), which is encouraging. It shows that the evolutionary algorithm is capable of finding functional forms bearing some resemblance to those available from first principles.

The trained models are therefore sensitive to rotation through the Q term (in the presence of MSVs) and, upon their detection, increase the anisotropy. This has an effect on vorticity production, see Eq. (7), which we have plotted in Fig. 13. The top half shows the production as a direct consequence of Eq. (12), whilst the bottom plane shows the actual vorticity production from the H-R/L. We can see that the modelled production mechanisms are very close to those actually observed, albeit the data is not fully converged. Note, Eq. (12) contains third order derivatives which take a considerable amount of time to converge. Despite this, as the finite time average is a Reynolds operator, our arguments still hold. The underpredictions close to the wall are due to the

⁷ The algorithm does not produce the algebraically simplified form of the equation.

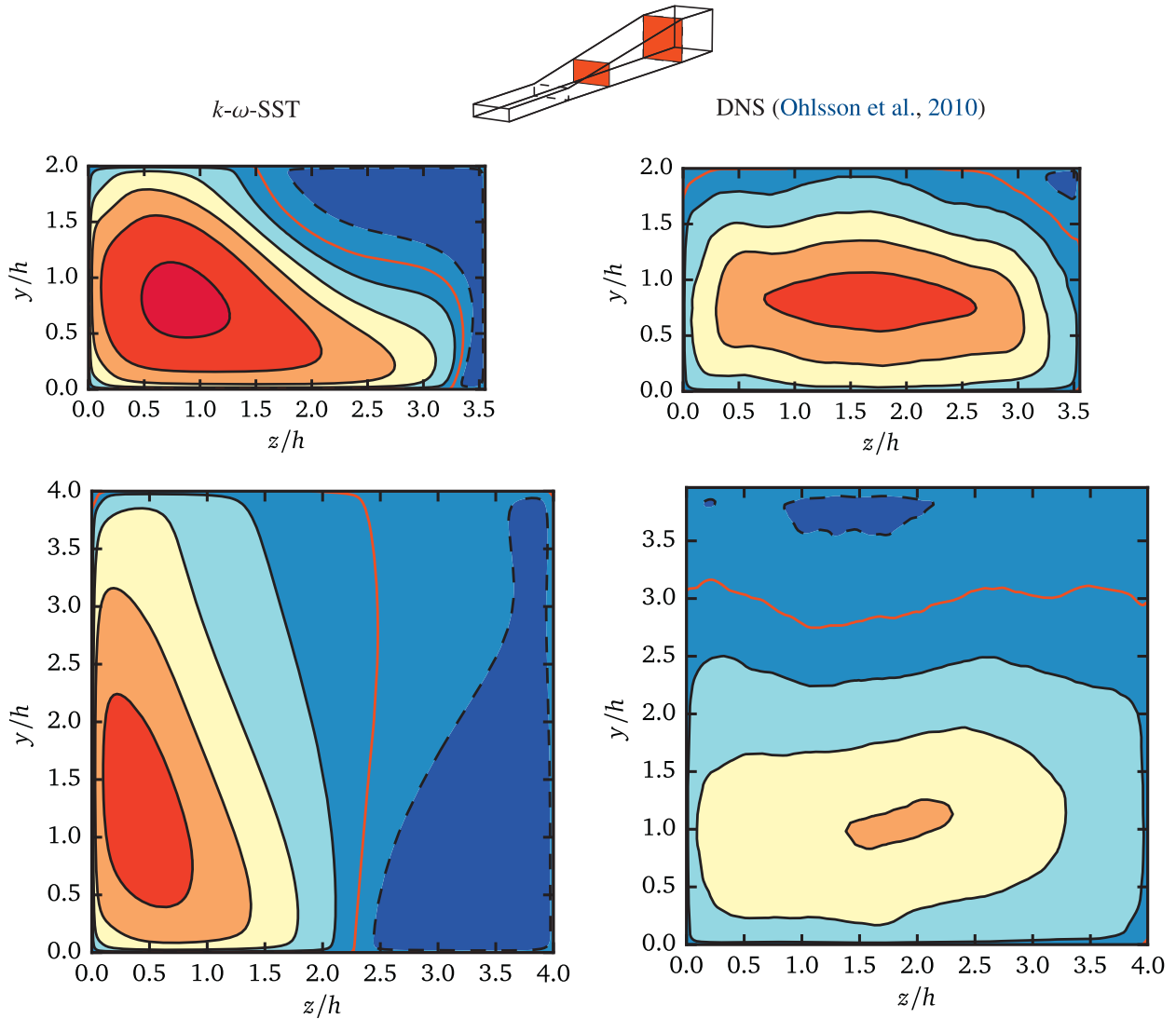


Fig. 9. Streamwise velocity U at $x/h = 5, 15$ for the DIFF case. (—) $U = 0$.

model dependency on τ_t .

The conclusion, given the magnitudes in the bulk, is that MSV persistence is actually a phenomenon related to the linear V_{ij}^1 component term, i.e. they are predominantly a straining process. Further, as there was no coherence in non-linear functional form, we conclude (rather tentatively) that V_{ij}^2 and V_{ij}^3 terms are only required for initialisation of MSVs and do not necessarily play a large role in the physical dynamics. This shows off one of the by products of a symbolic algorithm. We have observed the creation of a model component not prescribed by the user and from this, we have deduced physical interpretation of the modelling process.

6.3. The invariant map and correlation between training databases

To test the trained models' ability to reproduce the anisotropy of Reynolds stress, the invariant map is a useful measure (Lumley and Newman, 1977). The second and third invariants of a symmetric traceless tensor are,

$$II = -\frac{1}{2}a_{ij}a_{ij} \quad (16a)$$

$$III = \frac{1}{3}a_{ij}a_{jk}a_{ki}. \quad (16b)$$

The second invariant gives a measure of anisotropy, whilst the third describes the type. Because on the $III - II$ plane portions of the map can appear distorted, it is convenient to display the map in barycentric coordinates (Banerjee et al., 2007).

In Fig. 14, examples of this map are shown in the region $y, z < 0.4h$ of the VIN1 and CHY33 ducts. Colour intensity and size depict wall distance. We show the DNS VIN1 case as a comparison for the H-R/L, yet no similar plot is available for CHY33. The most striking contrast is the H-R/L inability to reproduce the near-wall state of anisotropy, because of the increase in modelled turbulent viscosity. Consequently, the one and two component states of turbulence are not achieved (see Simonsen and Krogstad (2005) for a discussion on this terminology).

The linear model, Eq. (1b), is applied to the frozen H-R/L data with minimal predictive accuracy. In this *a priori* test, ν_t is calculated using the H-R/L prediction of k and the frozen value of ω , whilst S_{ij} is calculated using the H-R/L velocity field. We see that proportionality with strain does not provide a significant departure from isotropy (the base of the triangle), with the modelled stress tensor neither hugging the axisymmetric expansion line nor reaching far along it. This is the case even though the model has been fed a more representative velocity field than it could itself predict (see Fig. 2).

Contrast this with the ensemble GEP predictions \tilde{V} and \tilde{C} , also

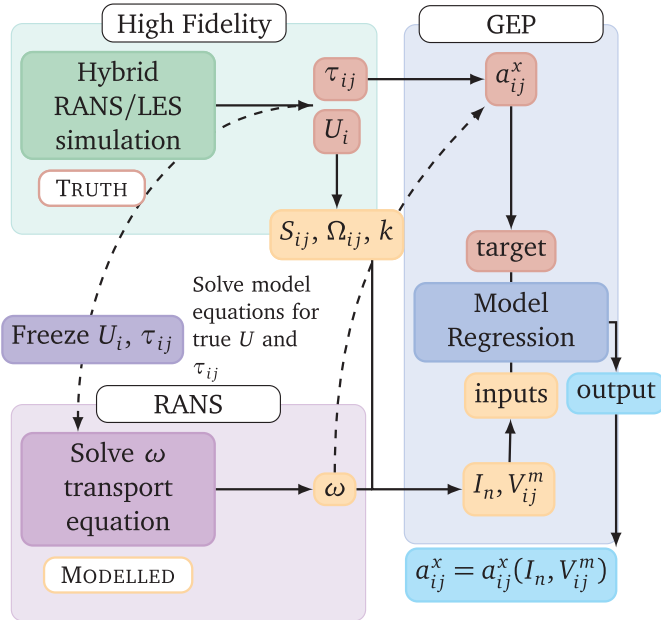


Fig. 10. Algorithm flow illustrating the input and target variables and the output functional form. The implementation is designed to fit ‘true’ anisotropy (output) with modelled quantities (input) for a given velocity field.

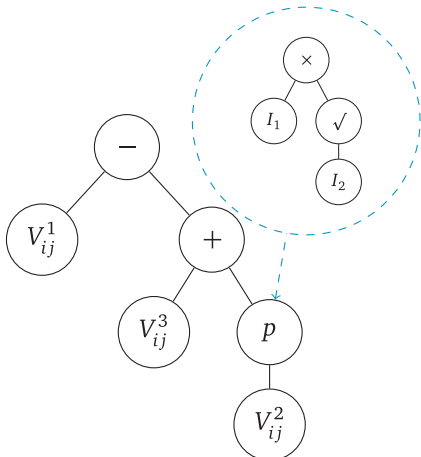


Fig. 11. Example ET.

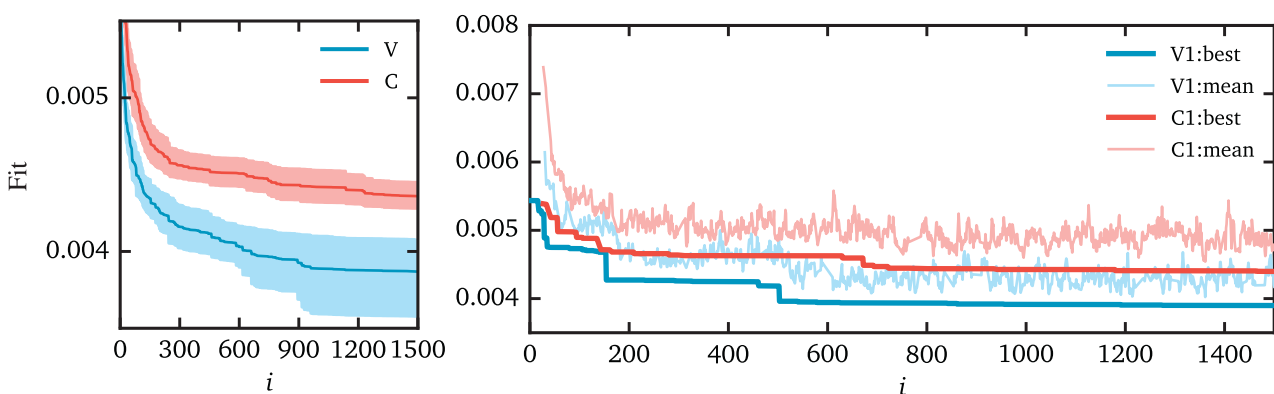


Fig. 12. Evolutionary algorithm performance. Left: mean best member from each population as a function of generation i . A 95% confidence interval for this quantity is reported. Right: example runs that produced models C1 and V1. Mean refers to the population mean, best is the population minimum and it is this quantity that contributes to the left plot.

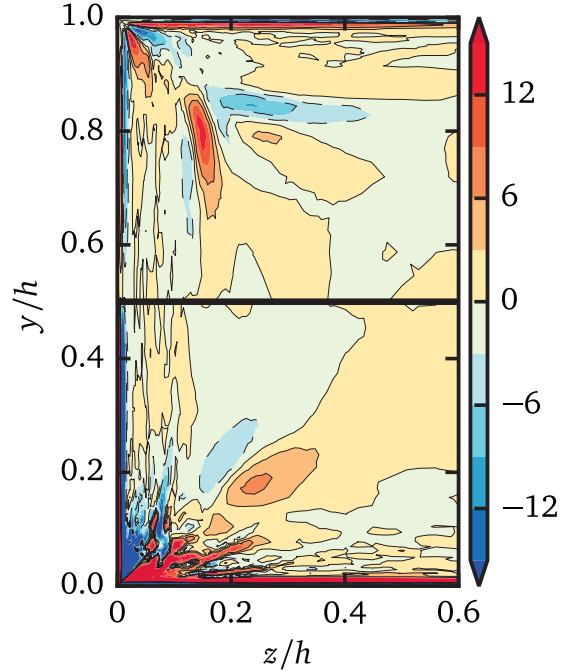


Fig. 13. Non-dimensional streamwise vorticity production in the left hand portion of the CHY33 duct. Top: from Eq. (12) (using the frozen H-R/L). Bottom: from H-R/L a_{ij} .

applied to H-R/L data. These models are the average prediction made by V1-15 and C1-15 respectively. The anisotropy is correctly captured away from the wall. This statement is true irrespective of the training case; Fig. 14 shows each model applied to both cases, in the manner outlined in Fig. 3. This *a priori* test shows very little dependence on the training data, with both models performing well for both duct geometries.

All models return to isotropy as the wall is approached, along the plane strain line indicated in red. This is true even for the GEP models, although this line is not reached until very close to the boundary. This is in clear contrast to the DNS result, which tends to the one component limit, via an axisymmetric expansion, before reaching a two component state at the wall. The reason for this qualitative error is due to the non-dimensionalisation by $\tau_t = 1/\omega$. The current choice of time scale tends to zero as the wall is approached. This implies that V_{ij}^k and I_k tend to zero and from Eq. (6) we see that a_{ij}^x is highly likely to vanish.⁸ Consequently, the machine learnt turbulence models tend to the linear model as the wall is approached.

⁸ We say highly likely, because it is possible to find an approximation to a function with limiting behaviour, although this is not probable.

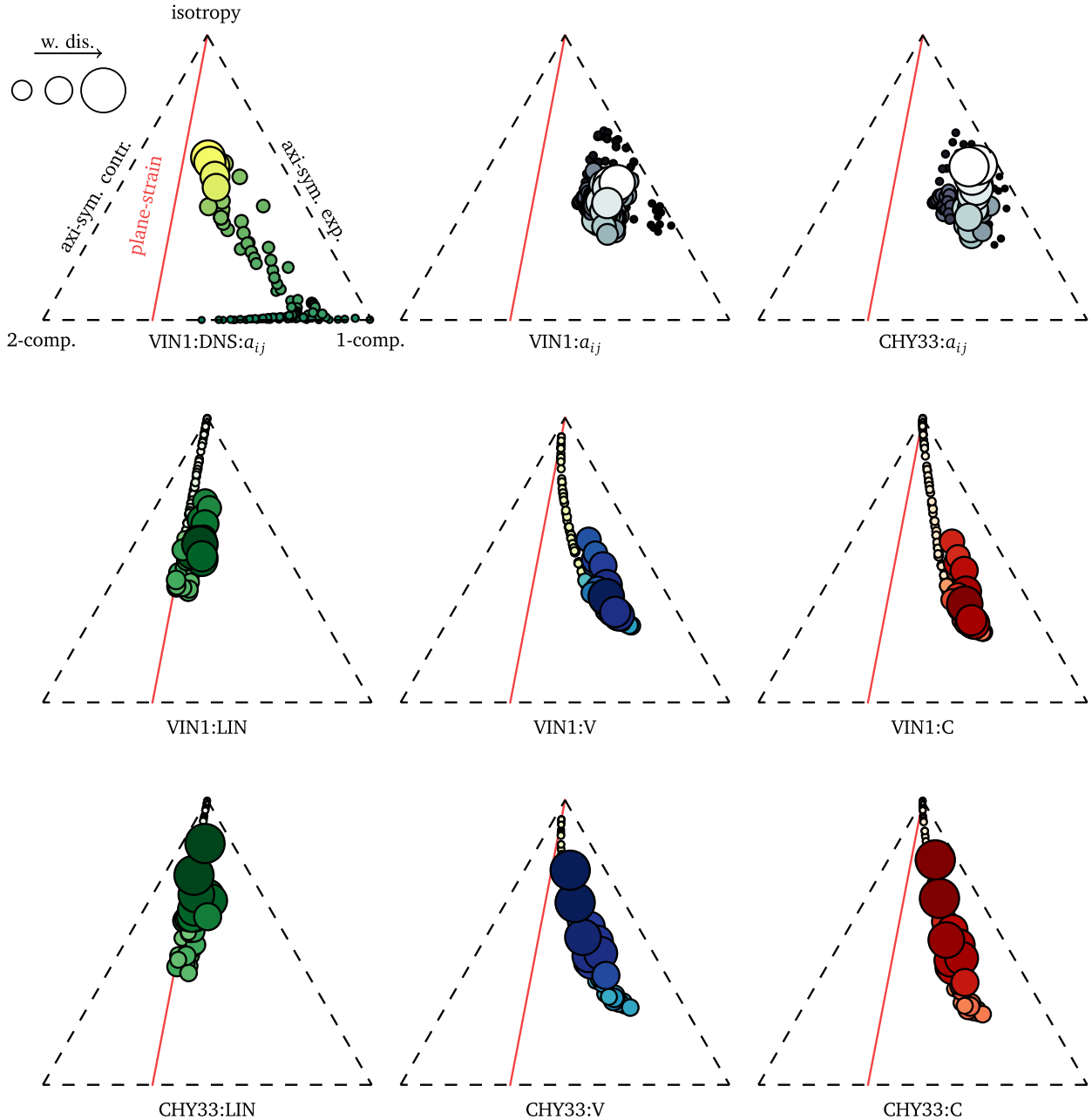


Fig. 14. Invariant maps in barycentric coordinates. Title of each plot denotes DATA:ANISOTROPY, where DATA is the data set used and ANISOTROPY is the tensor used to calculate the invariants. Exception to this naming is the DNS, other plots are implicitly H-R/L data. Symbols: (○) DNS (Vinuesa et al., 2014); (◐) H-R/L; (●) linear model (Eq. (1b)) applied to H-R/L; (●) \tilde{V} model applied to H-R/L; (●) \tilde{C} model applied to H-R/L. Symbols increase in size to denote distance from the wall. Data is extracted from the region $y, z < 0.4h$.

In order to quantify error, we transform to the $\xi - \eta$ space,

$$\eta = \left(\frac{-II}{3} \right)^{1/2} \quad (17a)$$

$$\xi = \left(\frac{III - II}{2} \right)^{1/3}. \quad (17b)$$

because in the $III - II$ plane, the departure from isotropy is a second order effect. We calculate the relative error for the CHY33 and VIN1 cases, denoted ϵ_c and ϵ_v respectively. The errors ϵ_c and ϵ_v are calculated as

$$\epsilon = \frac{1}{N} \sum \sqrt{\frac{(\eta^{\text{hrl}} - \eta^{\text{mod}})^2 + (\xi^{\text{hrl}} - \xi^{\text{mod}})^2}{(\eta^{\text{hrl}})^2 + (\xi^{\text{hrl}})^2}}, \quad (18)$$

where N is the total number of data points, which the summation is over. The mod superscript denotes the model in question. These errors are displayed in Fig. 15, where red denotes models trained on CHY33 and blue denotes models trained on VIN1. Green denotes the linear approximation (Eq. (1b)). Note that ϵ is not equivalent to Eq. (9), however one would hope that in minimising the objective, the error in predicting (ξ, η) is also reduced. The size of each data point (with the exception of the linear case) is scaled by fitness. By comparing blue points with ϵ_v and red with ϵ_c , a measure of the training phase is appreciated. In the main plot, we see that the ensemble predictions are

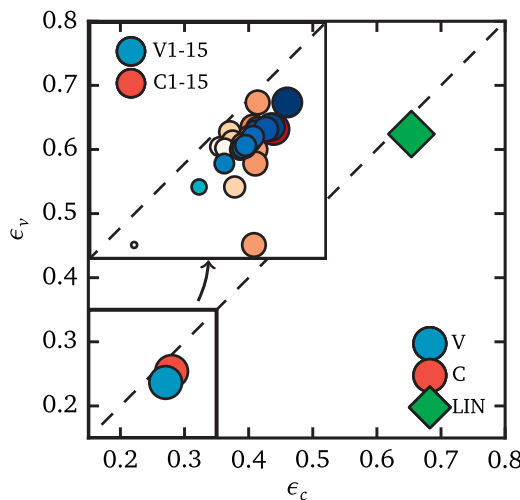


Fig. 15. Error in $\xi - \eta$ space. x axis is error in the CHY33 data set ϵ_c ; y axis is analogous for VIN1 data set ϵ_v . Each data point is a model, the main plot is of ensemble models and the linear relation Eq. (1b) and the inset shows individually trained models. Colours represent original training data set, sizes (inset only) are training fitness. (For interpretation of the references to colour in this figure legend, the reader is referred to the web version of this article.)

significantly better than the linear model for both cases. The line $\epsilon_v = \epsilon_c$ is shown as a visual reference and because both ensemble models lie close to this, we conclude that the evolved models using VIN1 can be successfully extrapolated to CHY33 and vice versa. This gives us confidence in applying trained models to similar, yet different geometries. Note both predictions satisfy $\epsilon_v < \epsilon_c$, again reiterating that Eq. (9) is easier to minimise for the VIN1 case.

The inset of Fig. 15 shows each of the models contributing to these ensemble predictions. Once more we see that $\epsilon_v < \epsilon_c$, however, we now observe our first training database dependency. The marker radius is a function of training fitness (Eq. (9)) and for V1-15, we see this correlates exceptionally with ϵ_v . Further, ϵ_v correlates extremely well with ϵ_c , implying that a predictable level of error is made in the $\xi - \eta$ plane for both cases and that this is a strong function of our objective. On the other hand, the information learnt by the C1-15 models in the CHY33 database is not transferred as well to the VIN1 case — evident by poor correlation between ϵ_c and ϵ_v . This is again, due to the symmetry in the flow enforcing along two lines⁹ $\tau_{22} = \tau_{33} \neq 0$, but $V_{\alpha\alpha}^1 = V_{\alpha\alpha}^1(\partial_{x_j} U_i) = 0$. Given that in Section 6.2, we showed that this term is important in the MSV dynamics, an error is induced in the EASM models as this term vanishes. For the VIN1 case, this symmetry region is a major source of error, yet for the CHY33 case, this region is proportionally smaller — being an asymmetric geometry — but the models make further errors away from these symmetry lines. Then, when C1-15 are applied to the VIN1 case, they no longer make their asymmetric error, but their symmetric error is exposed. This was not the main driver of fitness improvements, as the asymmetric error was larger and consequently, we observe unpredictability in the error made by C1-15 on VIN1. See the schematic of Fig. 16 for a visual explanation. This discussion aside, the errors made by the trained models *a priori* are small and such a test has been highly encouraging.

6.4. A posteriori implementation of P_k

Given the encouraging *a priori* validation in Section 6, in the next section we move onto *a posteriori* validation. That is, insert our new models V1-15, C1-15 into the $k - \omega$ -SST model as described in Section 2.

⁹ For the VIN1 case this is $y = \pm z$.

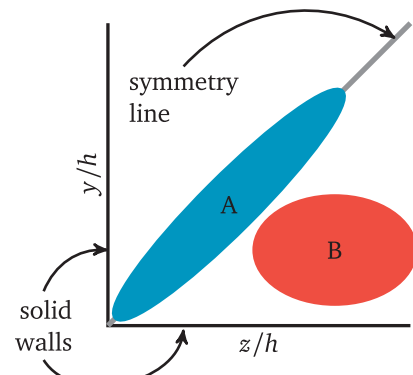


Fig. 16. Illustration of regions of error in the lower left quadrant of an arbitrary duct configuration. A: error induced by velocity gradients vanishing on symmetry lines. B: error induced by $\ell_x > \ell_y$. For CHY33 $|A| \ll |B|$, but for VIN1 $|A|$ and $|B|$ are significant.

The production term is often difficult to manage in turbulence models. For example, Menter (1992) and Kato and Launder (1993) have reported excessive turbulent kinetic energy production from very high shear levels. Instead proposals utilising the vorticity magnitude $\Omega = \sqrt{2\Omega_{ij}\Omega_{ij}}$ were argued. After some initial runs of our trained constitutive stress-strain relationships, we discovered an issue with the production term P_k . That is the linear coefficient $1 - \beta_1$, acted to hinder the production of the turbulence energy near the wall, as the MSV became fully developed. This resulted in a relaminarisation of the boundary layer and ‘lift off’ of the secondary structures. After enough iterations, the flow became unphysical and failed to converge to a steady state.

One major advantage that GEP has over other machine-learning frameworks currently being explored in the literature (e.g. Neural Networks) is the possibility for humans to inspect and, if needs be, modify the model. This is because the result is a tangible expression. We remind the reader that the end goal of this method is a model that works and can be applied. As we discussed above, our approach is ‘maximally empirical’ and can claim no groundings in physical arguments — rather relying on inference. It must also be acknowledged that modification/enhancement is a common practice in conventional turbulence model development, often very *ad hoc* and by a simple comparison to data. We make such a modification below.

As our method is allowed to modify the effective viscosity

$$\nu_t + \nu - 2k\tau_l\beta_1, \quad (19)$$

where β_1 is the V_{ij}^1 coefficient from a_{ij}^x in Eq. (1d), we ensure that the strain term in the production does not become too low as the wall is approached by defining,

$$P_k = (1 + \|\beta_1\|)\nu_t S^2 - 2k(\beta_2 V_{ij}^2 + \beta_3 V_{ij}^3)S_{ij}. \quad (20)$$

$S = \sqrt{2S_{ij}S_{ij}}$ is the strain rate magnitude analogous to Ω . This equation also tries to limit excessive production, because whereas ν_t is limited in the $k - \omega$ -SST model,

$$\nu_t = \frac{a_1 k}{\max[a_1 \omega, F_2 S]}, \quad (21)$$

where $a_1 = 0.31$ and F_2 is the standard blending function, $k\tau_l \sim \nu_t$ is not. Also, we take $\|\beta_1\|$ because the linear model and this term can ‘compete’ with each other and cancel strain production entirely.

In Fig. 17, the standard and modified production terms have been calculated using the H-R/L data along a 45° line from the duct corner. One can see that the modified term matches the true production in the near-wall region but must accept excessive values slightly further out. This is in contrast to the standard term which under predicts everywhere.

This modification to the model is made in the P_k term only. It is clear our current objective function is unable to find an a_{ij}^x that is

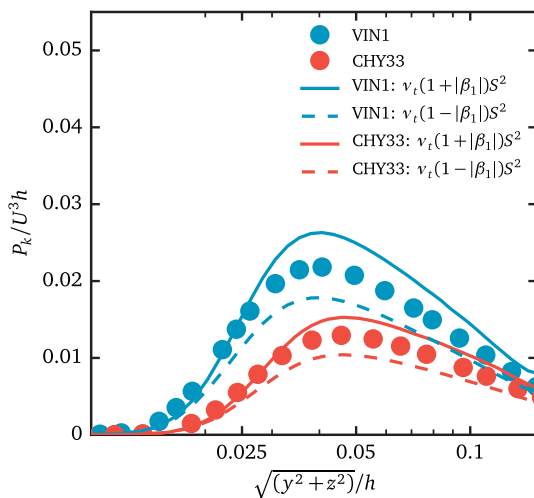


Fig. 17. Non-dimensional production of turbulent kinetic energy.

suitable for all parts of the RANS system of equations. This indicates that perhaps a multi-objective optimisation is required, to account for the projection of a_{ij}^x in the strain field and also for its derivatives. The first objective would take care of P_k and the second would address momentum diffusion. Such a multi-objective study is beyond the scope of this paper.

7. CFD test results

In terms of numerical convergence, only two models failed to converge to a steady solution for *all* geometries tested. This excellent probability of numerical stability was also found in a previous study (Weatheritt and Sandberg, 2016c) and here we lend further evidence of successful calculations using evolved functional forms in CFD codes.

That is V6, given by Eq. (10), did not converge as hypothesised above but did not diverge either. By non-convergence we mean that no steady state was reached in a reasonable number of iterations (for the VIN1 case, the simulation was halted after 3×10^5 iterations). Being the fittest model from the VIN1 training database, this is an example of ‘overfitting’ the data, where the algorithm has produced a vastly complex functional form in order for small improvements in training performance. This kind of function then does not sit well with the CFD solver. The other model that did not converge, C7 given by,

$$\begin{aligned} a_{ij}^x = & 2V_{ij}^1 I_2^{-I_2+\exp(I_2)}(I_1(2I_2-1)+I_2-2) \\ & + V_{ij}^2 \log(I_1(I_1+\log(-0.89\log(I_1-I_2))-1)) \\ & + 2V_{ij}^3 \exp(0.057I_1+0.114I_2+1.05073) \end{aligned} \quad (22)$$

diverged after the first iteration because of the V_{ij}^1 coefficient. The exponent was enough for a floating point exception and we doubt that this term would remain finite for many flow fields. Consider that because $I_2 \leq 0$, the V_{ij}^1 coefficient is $\propto I_2^{|I_2|}$. Whilst it remained so when calculated on the high-fidelity data, the development of the RANS solution (from rest¹⁰) caused divergence. The ultimate goal of this work is to produce CFD friendly turbulence closures and therefore we refrain from deviating from standard numerical schemes and initial conditions and conclude that this model is of no practical use. **This is another example of complex functional forms causing issues. However, as our algorithm is symbolic, we can inspect these terms and diagnose potential issues.**

The remaining 28 models are now discussed on a case by case basis.

In order for a comparison, we also ran an EASM

model (Weinmann and Sandberg, 2009) based on the Speziale et al. (1991) pressure-strain correlation, which we denote SSG. This comparison will show that the addition of non-linear terms is not a guarantee of the performance increases we can demonstrate with our trained models. Note, we do not consider a linear RANS case, as it does not predict MSVs — see Fig. 2 — so the reader should bear this in mind when evaluating the non-linear extensions.

7.1. Cases: VIN1, VIN7, CHY33

To show the flow features present in the ducts we have plotted the streamwise velocity U/U_b and spanwise velocity magnitude $\sqrt{V^2 + W^2}/U_b$ of the three duct configurations in Fig. 18 and Fig. 19 respectively. To avoid drowning in contour plots, we restrict the data to the best model from each trained set, V13 and C14 given by the respective equations,

$$\begin{aligned} a_{ij}^x = & 2I_1 V_{ij}^1 (4I_1 - 2I_2 + (I_1 - I_2)^2 + 2) \\ & + V_{ij}^2 (2.945I_1 - 1.68 - \log(I_1))\log(I_1) \\ & - V_{ij}^3 (\log(I_1(2I_1 - I_2)(\exp(-I_2) + 2)) + 2) \end{aligned} \quad (V13) \quad (23a)$$

$$\begin{aligned} a_{ij}^x = & 2I_2 V_{ij}^1 (2 - I_2)(2I_2 - 1) \\ & + V_{ij}^2 (\log(9I_2^2) + \tanh(2I_1) - 1) \\ & + V_{ij}^3 ((I_2 + 2)^2 + 2). \end{aligned} \quad (C14) \quad (23b)$$

In addition, the reference DNS and the companion SSG RANS are included. The schematic in each figure shows which quadrant corresponds to which methodology. These three ducts therefore represent, for each model, a case they have been trained on, a case they have been *a priori* tested on and a case previously unseen (VIN7). For CHY33 and VIN7, Fig. 18 illustrates a generous pinching of the mean streamwise velocity contours by V13 and C14, yet the bulk flow is centred too narrowly. This hints at MSVs that penetrate too far and this can be confirmed by considering the cross flow magnitude in Fig. 19. On the contrary the SSG is much too weak, barely deflecting the mean flow in each duct and, if we consider the cross flow, we can see much too weak MSVs.

For the VIN1 case, V13 and C14 give very good predictions of the shape and extent of the energetic side of the MSV. Fig. 19 shows the three lobes of peak cross flow magnitude are well predicted topologically, however, the magnitude is slightly too low. This means that the streamwise velocity contour Fig. 18 is not ‘square’ enough.

Common to all geometries, the trained models have over responded to the shear along the lines $z/h = 1/2$ (and $y/h = 1/2$ in the VIN1 case). This manifests as a too large W/U_b component. This implicates the MSVs are too elongated and not anchored close enough to the shorter wall. It is currently unclear as to what is causing this, possibly the homogeneous turbulence assumption made in using Eq. (2), but note that the flow topology is similar for the SSG — so we do not suppose the issue is inherent to the GEP approach.

Of obvious engineering value is the strength of the MSVs and the quality of this prediction. For this, the area-averaged mean streamwise enstrophy contribution

$$\mathcal{E} = \frac{1}{\ell_y \ell_z} \int_0^{\ell_z} \int_0^{\ell_y} (\epsilon_{ijk} \partial_j U_k) (\epsilon_{ilm} \partial_l U_m) dx dy, \quad (24)$$

is calculated, for the VIN1 and VIN7 cases. \mathcal{E} provides an integral quantity that gives us some insight into the global quality of our RANS solutions. The result is plotted in Fig. 20, the total enstrophy from the VIN1 case along the x -axis and similarly for the VIN7 case along the y -axis. We include the SSG and linear models also, along with the DNS. Firstly, we can see that the trained models are markedly better than the SSG model, which performs only slightly better than the linear prediction of $\mathcal{E}_{VIN1} = \mathcal{E}_{VIN7} \equiv 0$. This plot quantifies the improved quality of our entire set of trained models over the linear and established EASM

¹⁰ We also attempted from the linear solution.

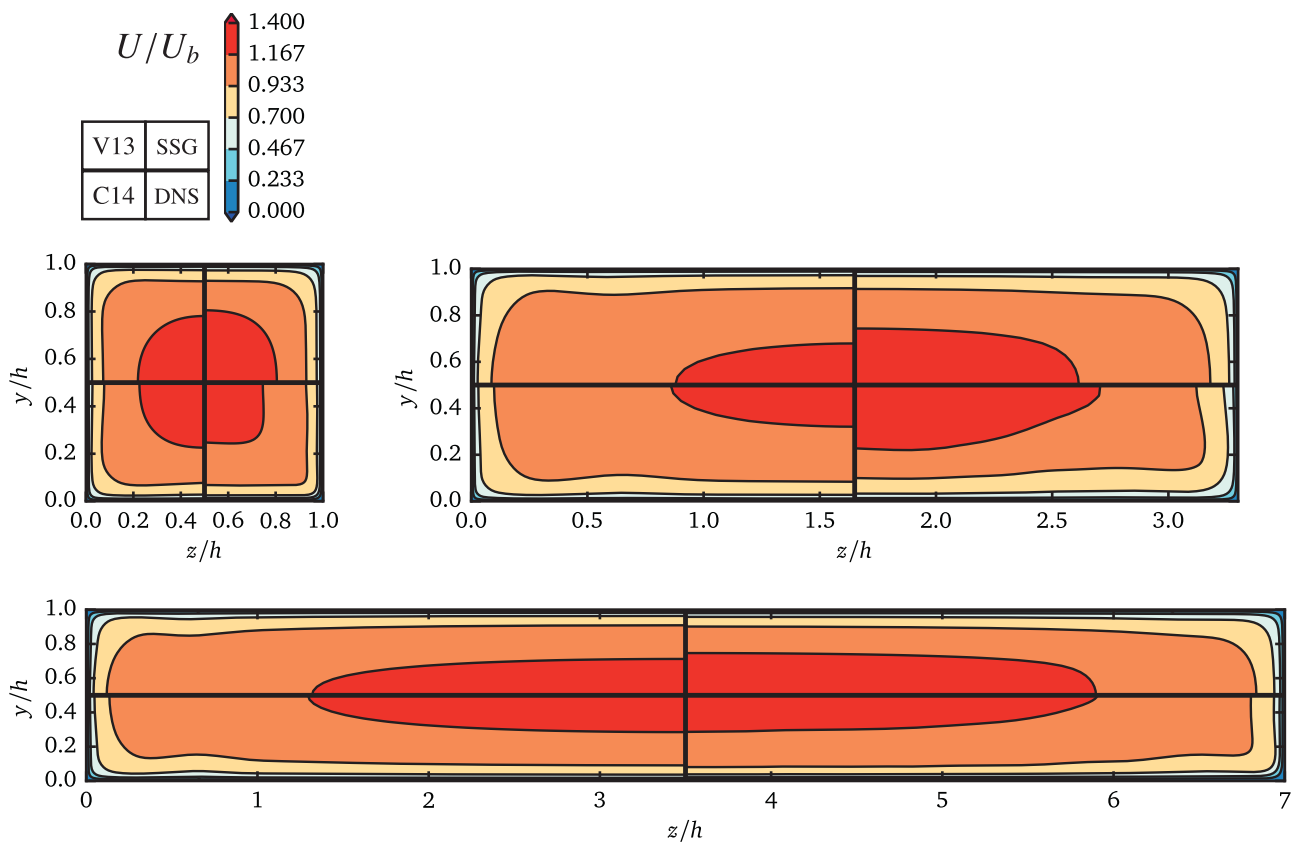


Fig. 18. Contours of streamwise velocity U/U_b . The schematic shows which methodology is depicted in which quadrant. The ducts are in clockwise order from the top left: VIN1, CHY33, VIN7.

closures. Aside from the two that did not converge, every single one of our closures improved prediction.

Conversely, during *a posteriori* testing, the VIN1 case is now much more tricky than the VIN7. This is because, despite the physics being trickier in the VIN7 duct, the MSVs occupy a smaller fraction of the domain. The magnitude of \mathcal{E} in the VIN7 duct is very encouraging; the better models are predicting this quantity within 1% and the worst are a 65% decrease on the DNS. The enstrophy predicted by the SSG, on the other hand, is 97% too small.

The dashed line included in Fig. 20 is the equation

$$\mathcal{E}_{\text{VIN1}} = 6\mathcal{E}_{\text{VIN7}} \approx 7\mathcal{E}_{\text{VIN7}}, \quad (25)$$

which is $A_1 \mathcal{E}_{\text{VIN1}} \approx A_7 \mathcal{E}_{\text{VIN7}}$, where $A_{1,7}$ are the cross sectional areas of the VIN1 and VIN7 ducts. That the trained models lie almost perfectly on this line yields a few interesting comments. Firstly, there is consistency between the cases and the relation between the enstrophy of the two cases is linear. It is vital in machine-learning studies to ensure that your model is a useful predictive tool by testing on unseen data. That the correlation between the two cases is extremely high, at values of $R = 0.87$ and $R = 0.97$ for the C1-15 and V1-15 models respectively, where R is the Pearson correlation coefficient, implies credibility for, and confidence using, our trained models. Should this correlation be low, then we could place no faith in our models when predicting new geometries. Instead, we have confidence and we are able to make a back of an envelope style approximation of the error for at least similar style duct cases. Secondly, the coefficient of proportionality is close to the duct area proportionality. This implies our trained models are not functions of the Reynolds number of the flow that they were trained upon, this is seen by considering the VIN7 Reynolds number is half that of the other duct geometries. This observation is by no means conclusive, but is encouraging, as Reynolds number effects are often cited as a major issue when developing generalisable turbulence

models (e.g. Leschziner, 2015). The final comment is slightly puzzling and currently, we can only leave it as a passing remark. That is no model predicts the absolute magnitude of $\mathcal{E}_{\text{VIN1}}$ case well. At this stage we postulate that the error is relative to the inherent modelling assumption of Eq. (1c); that is under vanishing velocity gradient, the anisotropy also vanishes. The area of this violation is significantly higher for the VIN1 case. Perhaps the issue could also be related to the $k - \omega$ transport equations or perhaps an error that is induced from assuming weak equilibrium — which falls down in regions of strong gradients of the Reynolds stress — inherent in the EASM framework. This postulation is left open at the time of writing, however, is an avenue of present exploration.

In order to quantitatively view all the trained models, we have plotted the spanwise velocity components for the VIN1 and VIN7 cases in Fig. 22. The profiles demonstrate the improved prediction in the lateral velocity components and the consistency of the models produced by GEP. The ensemble average prediction for each class of model \tilde{V} and \tilde{C} is surrounded by a 90% confidence interval for this mean. One can see a superior prediction over the SSG for even for the worst extreme of these confidence intervals, except the W component in the VIN7 duct, where the models are comparable. This reliability is pleasing, it allows us to have confidence in our turbulence models for a given class of flow.

We chose the profiles in Fig. 22 to intersect the region of strong negative W in the VIN7 case, where the asymmetry in the geometry is felt most. In this region the C models, trained on an asymmetric duct, perform better than the V models - which contained no experience of such a scenario from training. Conversely, the V models outperform the C upon the VIN1 case — precisely their training data.

We close the scrutiny of the duct cases via a return to the invariant map in $\xi - \eta$ space (See Section 6). Fig. 21 is the *a posteriori* companion to Fig. 14, using the data $y < 0.4h$, $z < 3h$. The case we consider is the VIN7 duct, the previously unseen geometry. Instead of comparing to

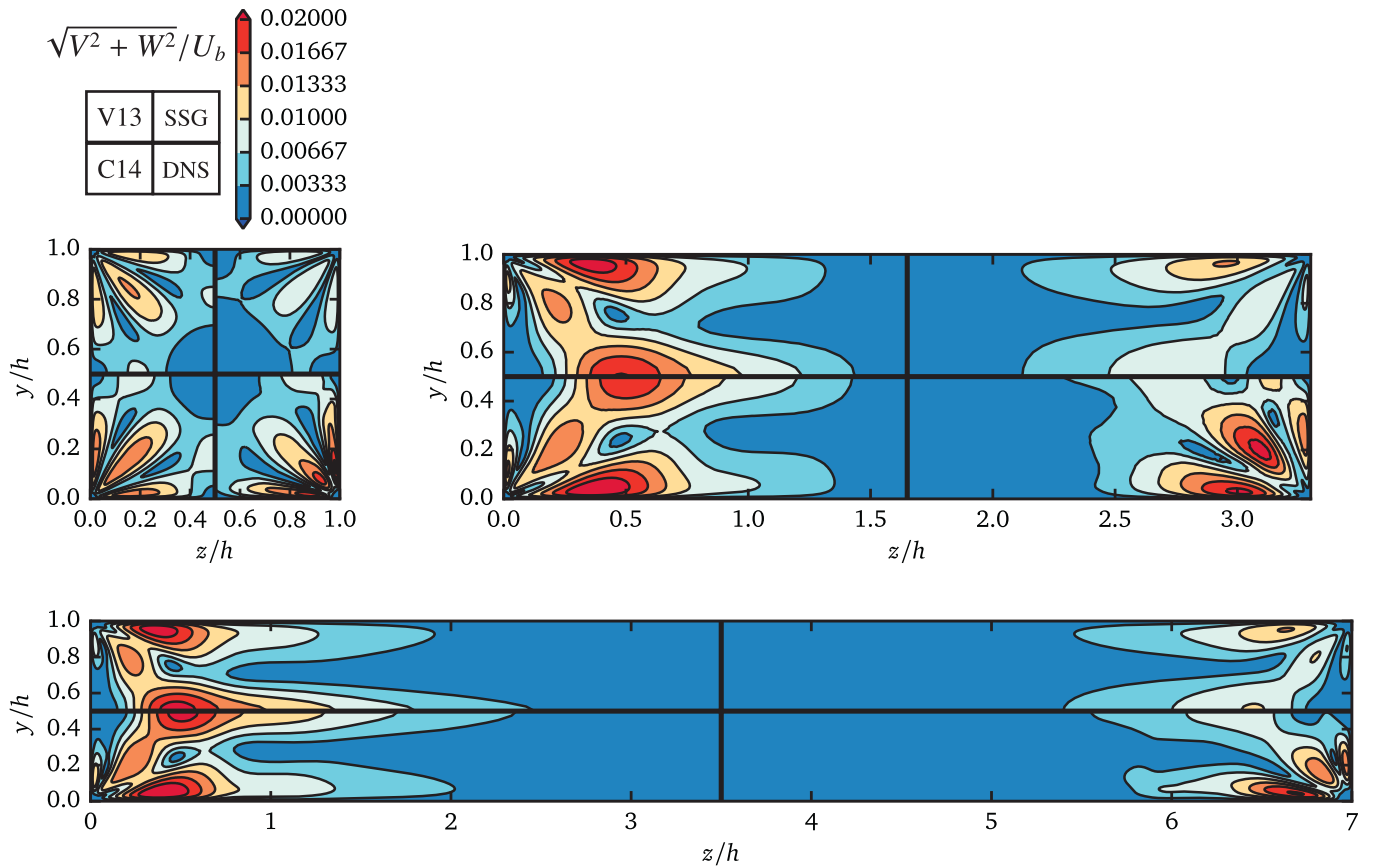


Fig. 19. Contours of spanwise velocity magnitude $\sqrt{V^2 + W^2}/U_b$. The schematic shows which methodology is depicted in which quadrant. The ducts are in clockwise order from the top left: VIN1, CHY33, VIN7.

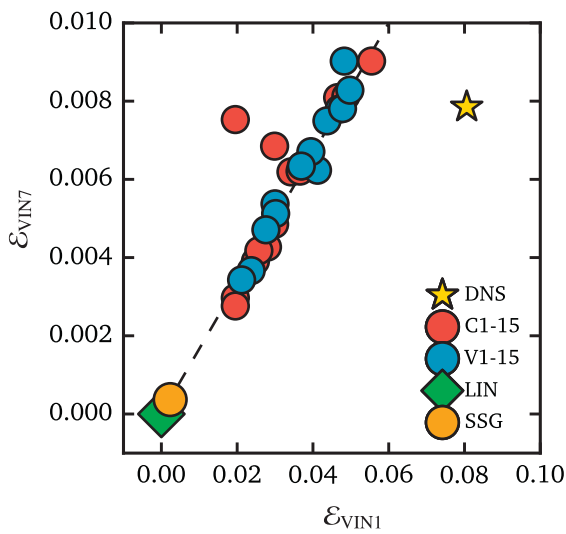


Fig. 20. Plot of streamwise enstrophy component ϵ for the VIN7 duct against the VIN1. Each data point is two simulations, described by the legend.

Eq. (1b), as in [Section 6](#), we benchmark against the SSG closure. Because the linear model fails to predict MSVs, the flow field is two-dimensional and consequently $III = 0$. This means that the linear model would follow the line of plane strain and is thus in great error when comparing to the DNS. Once again, as with the *a priori* testing, the EASMs return to isotropy in the near-wall region. However, the ensemble models contain an enhanced near-wall anisotropy relative to the SSG, seen by the tighter conformance with the axisymmetric expansion

line. We also see the effect of the reducing velocity gradients in the bulk; the invariant map caterpillars reverse their direction as the symbols increase in size, reflecting a greater wall distance. The \tilde{V} and \tilde{C} models achieve a much higher level of anisotropy than the SSG before this reversal and even contain a region sufficiently far from the wall and symmetry lines where they predict the correct state of anisotropy. This region is the lower part of the \tilde{C} and \tilde{V} invariant map and corresponds to the region $0.1h \lesssim \sqrt{y^2 + z^2} \lesssim 0.3h$.

7.2. Case: DIFF

This case is more expensive than the ducts discussed in the previous section. Given this, we decided not to run 30 RANS cases of this geometry. Instead we chose the first two models from each sample to give an impression of the predictive capability of the new models on a geometry that is much more challenging than their training case. This diffuser not only contains MSVs, but flow separation and an extended adverse pressure gradient, which is entirely new physics for the trained models. For reference we use both the experimental ([Cherry et al., 2008; 2009](#)) and DNS ([Ohlsson et al., 2010](#)) data because there are some visible differences between the two. Secondly, we use the results from a previous RANS study by [Schütze et al. \(2012\)](#) using the [Wallin and Johansson \(2000\)](#) model implemented in the NUMECA CFD package. This RANS study is included here, denoted as WJ, to give the reader an impression of the quality of our results.

The two tested models from our framework, V1 and C1, are given by the respective equations,

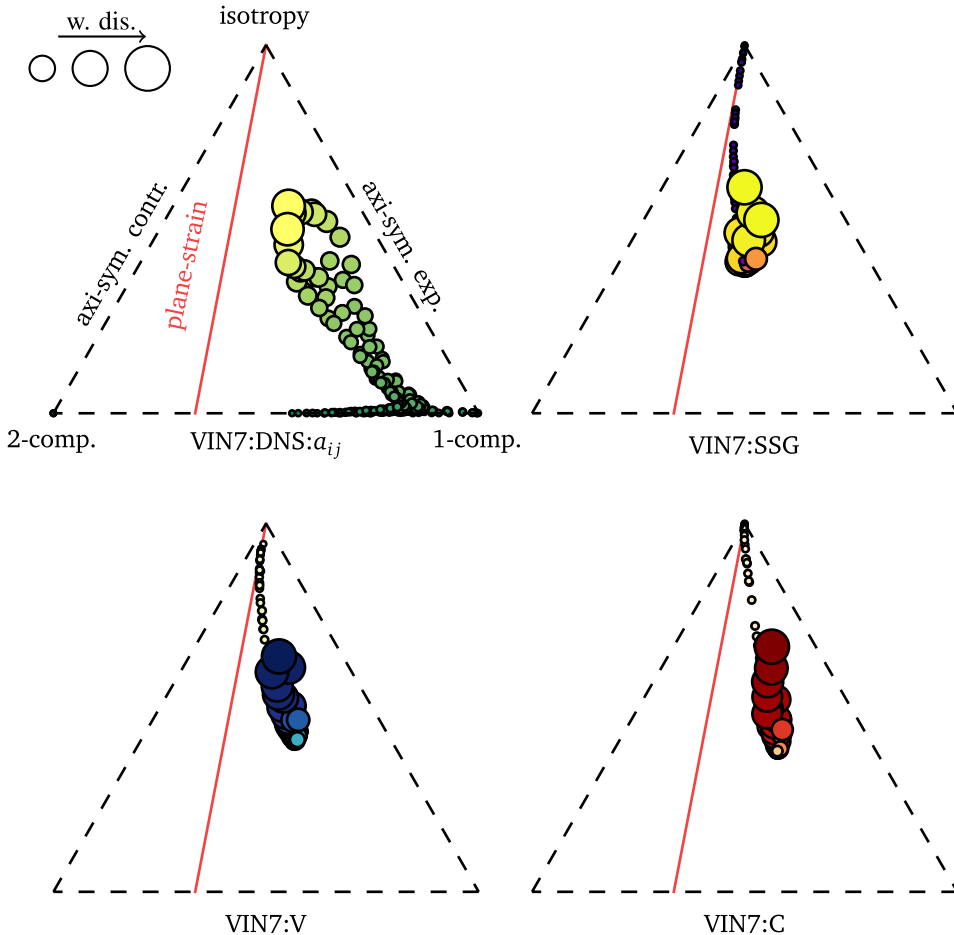


Fig. 21. Invariant maps in barycentric coordinates. Title of each plot denotes DATA:ANISOTROPY, where DATA is the data set used and ANISOTROPY is the tensor used to calculate the invariants. All plots are full CFD simulations. Symbols: (●) DNS (Vinuesa et al., 2014); (○) SSG model; (●) \tilde{V} model applied to H-R/L; (●) \tilde{C} model applied to H-R/L. Symbols increase in size and colour intensity to denote distance from the wall. Data is extracted from the region $y < 0.4h, z < 3h$.

$$\begin{aligned} a_{ij}^x = & V_{ij}^1(I_1 - 3I_2) \\ & + V_{ij}^2(\log(I_1^2 \exp(2I_1 - 8I_2 + 0.99)) - 2I_2) \\ & + V_{ij}^3(I_2 - \log(0.44I_1) + 2) \end{aligned} \quad (\text{V1}) \quad (26\text{a})$$

$$\begin{aligned} a_{ij}^x = & V_{ij}^1(2I_1^2 - 4I_2) \\ & + V_{ij}^2(2I_1 \exp(I_2 - 0.99) + \log(I_1(I_1 - 2I_2 - 0.01))) \\ & + V_{ij}^3(I_2 - I_1 + 6.01). \end{aligned} \quad (\text{C1}) \quad (26\text{b})$$

We chose the first two in an attempt to avoid bias in our selection. It is not unreasonable to assume that in industrial applications the first model produced from the algorithm would be used.

In order to visualise the flow through the diffuser, contours of streamwise velocity are plotted in Fig. 23 at five streamwise locations. The schematic shows these locations along the expansion. To further highlight the flow topology, the contour line $U = 0$ is emphasised in red. Note that the WJ contour lines are digitised from the original report (Schütze et al., 2012) using a k-means clustering algorithm (e.g. MacQueen, 1967) to first reduce the number of colours in the contour and then each pixel was binned according to a well known colour distance formula (Sharma et al., 2005). Care was taken to ensure the algorithm has properly identified $U = 0$. Note, the original colour map used by the authors was not perceptually monotonic and consequently there are a few pixels in the $0.6 \leq U/U_b < 0.8$ that have been incorrectly identified as $U/U_b > 0.8$ — which form a ring in the centre of this contour which the reader can safely ignore.

By considering the experimental or DNS data, one appreciates that the separation bubble appears predominantly in the upper right expanding corner. The shape of the inlet produces $U_z > U_y$ and this helps the flow ‘stick’ to this side. Consequently as one moves downstream, the reverse flow region grows along the upper surface. Contrast this with the linear prediction in Fig. 9, for which the flow separates along the side wall. In comparison, our C1 and V1 models are excellent predictors of the overall flow topology, especially in comparison to the WJ prediction. The WJ predicts a too strong early separation and what appears to be the persistence of the upper right MSV which acts to roll the flow up. This behaviour is seen somewhat to a lesser extent in the C1 prediction, but the V1 model handles the separation region extremely well. Note, the experiment would appear to have intermittent separation in the bottom right corner at $x = 15h$. This is not captured by any of the RANS models or the DNS. We are unsure if this is a result of some anomaly in the experimental results, most clearly seen in Fig. 24, which we should ignore, or whether this is real. In what we assume is a related phenomenon, the maximum in velocity shifts slowly to the left as it moves downstream. This may be an artefact of using MRI to gather data, but we note that this shift is seen to a stronger degree using the RANS models, yet not at all in the DNS.

Also provided for reference by the experimentalists, is the streamwise turbulence intensity $\sqrt{\tau_1}/U_b$, which we plot in Fig. 24. The sampling locations and ordering of the models are the same as in Fig. 23. Turbulence largely grows from the upper right corner in the

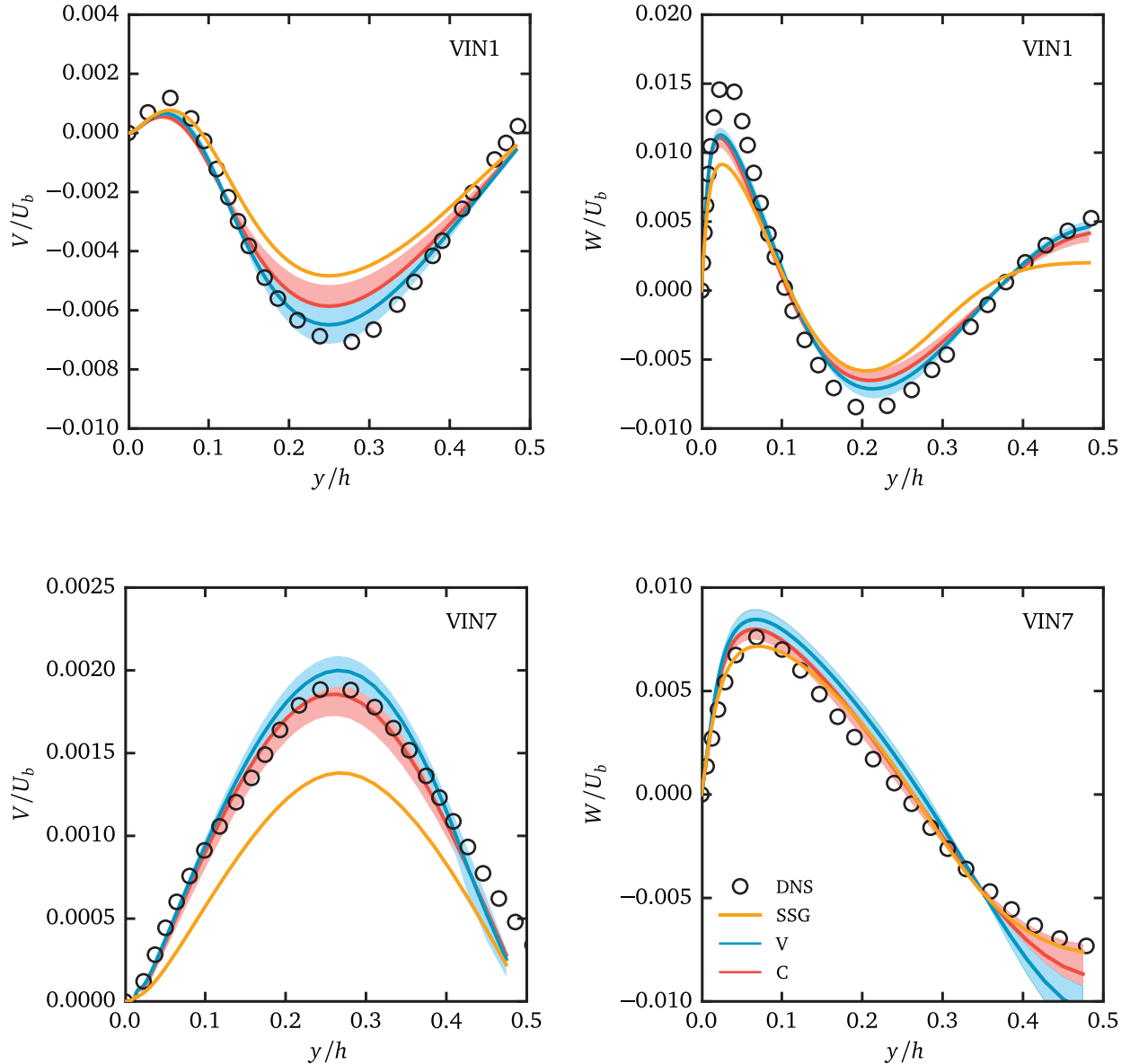


Fig. 22. Velocity profiles along $z = h/4$ for the VIN1 case and $z = h/8$ for VIN7. The V and C models are represented by their sample means and respective 90% confidence intervals.

recirculation zone and then wraps around the expanding walls as it convects downstream. The overall prediction made by C1 and V1 is excellent, especially when considering the WJ model entirely twists the mean field. As with the models considered in the full report (Schütze et al., 2012), the turbulence does not dissipate downstream sufficiently and the largely elliptical shape of the bulk $\sqrt{\tau_{11}}/U_b$, is not transported appropriately.

In order to measure absolute performance, the surface pressure coefficient $C_p=2(p-p_{\text{ref}})/U_b^2$ along the lower non-expanding surface is plotted in Fig. 25. C_p is calculated using the pressure on the surface at $x/h = 0.05$ and the average velocity at the diffuser inlet. Note we do not apply the correction used by Ohlsson et al. (2010). This plot firstly highlights the complete failure of the linear $k - \omega$ -SST model to predict this quantity and the need for more complex modelling approaches to calculate even simple statistical quantities. The EASMs capture the general flow field well. Of these, V1 is superior and both evolved models perform better than WJ. The V1 result should not be underestimated, the result is in excellent agreement with the reference data — especially considering this is a steady RANS calculation.

8. Conclusions and extensions

In this work we have demonstrated, through a two stage validation process, the current capabilities of machine-learning symbolic expressions for models of anisotropy. This paper has incorporated a modelling of the time scale by freezing the H-R/L velocity and stress fields. The main area of focus has been upon flow configurations that are difficult for standard industrial closures: by learning an anisotropy field underlying an MSV, then extrapolating these models to new geometries. The first stage of validation was *a priori*, demonstrating that the models can use high-fidelity velocity gradients to model the Reynolds-stress. The second step was a full implementation of the model into OpenFOAM and converging all differential equations from initial conditions. That only two models diverged is highly encouraging.

This extrapolation to newer, more difficult geometries — as with the diffuser — is vital for the framework to be industrially relevant. The reason the linear model prevails today is in part due to its robustness and this is a quality we must retain. That we have shown models that not only exhibit excellent predictions in the diffuser but appear robust

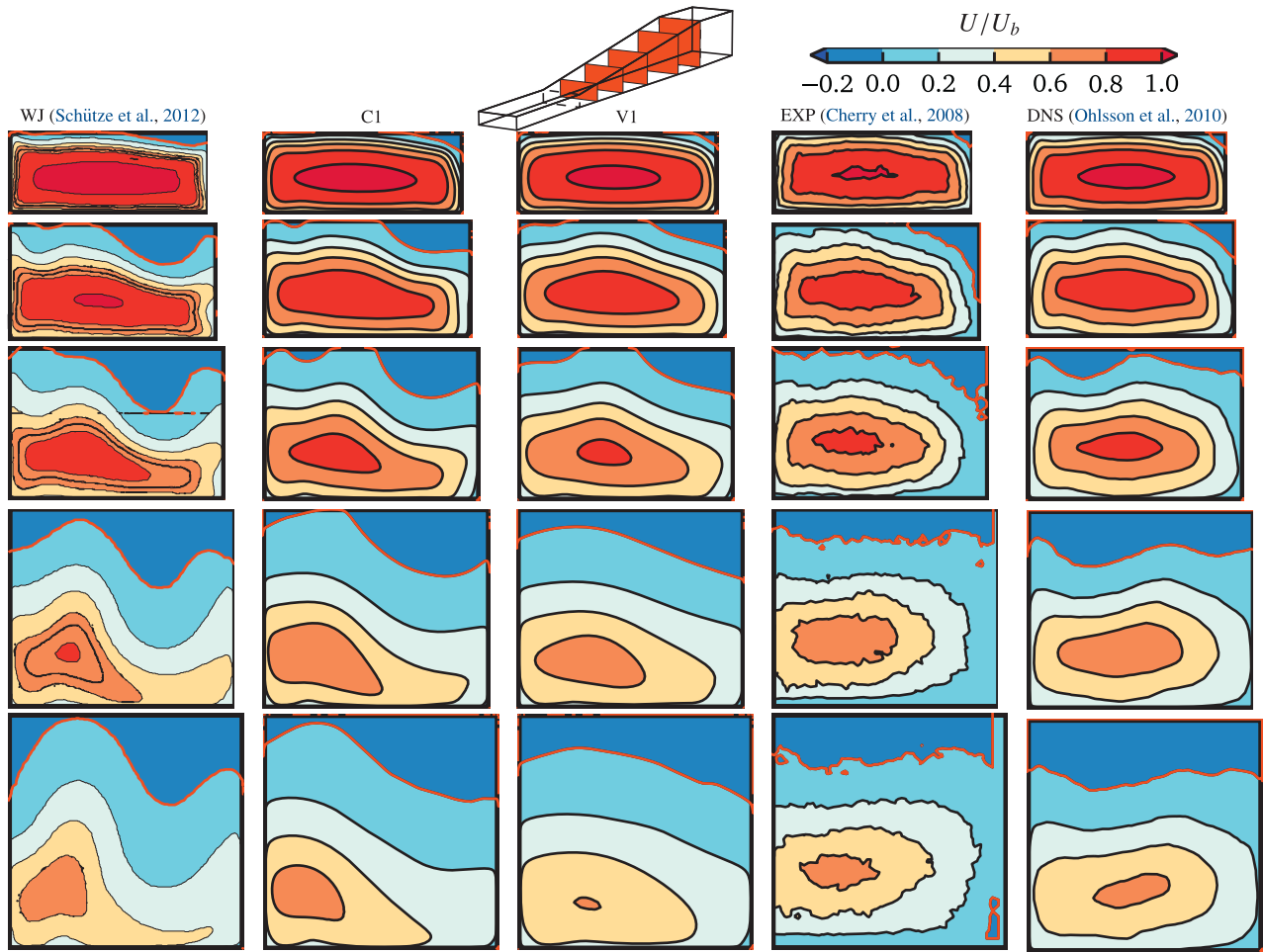


Fig. 23. Streamwise velocity at $x/h = 2, 5, 8, 12, 15$ for the DIFF case. (—) $U = 0$.

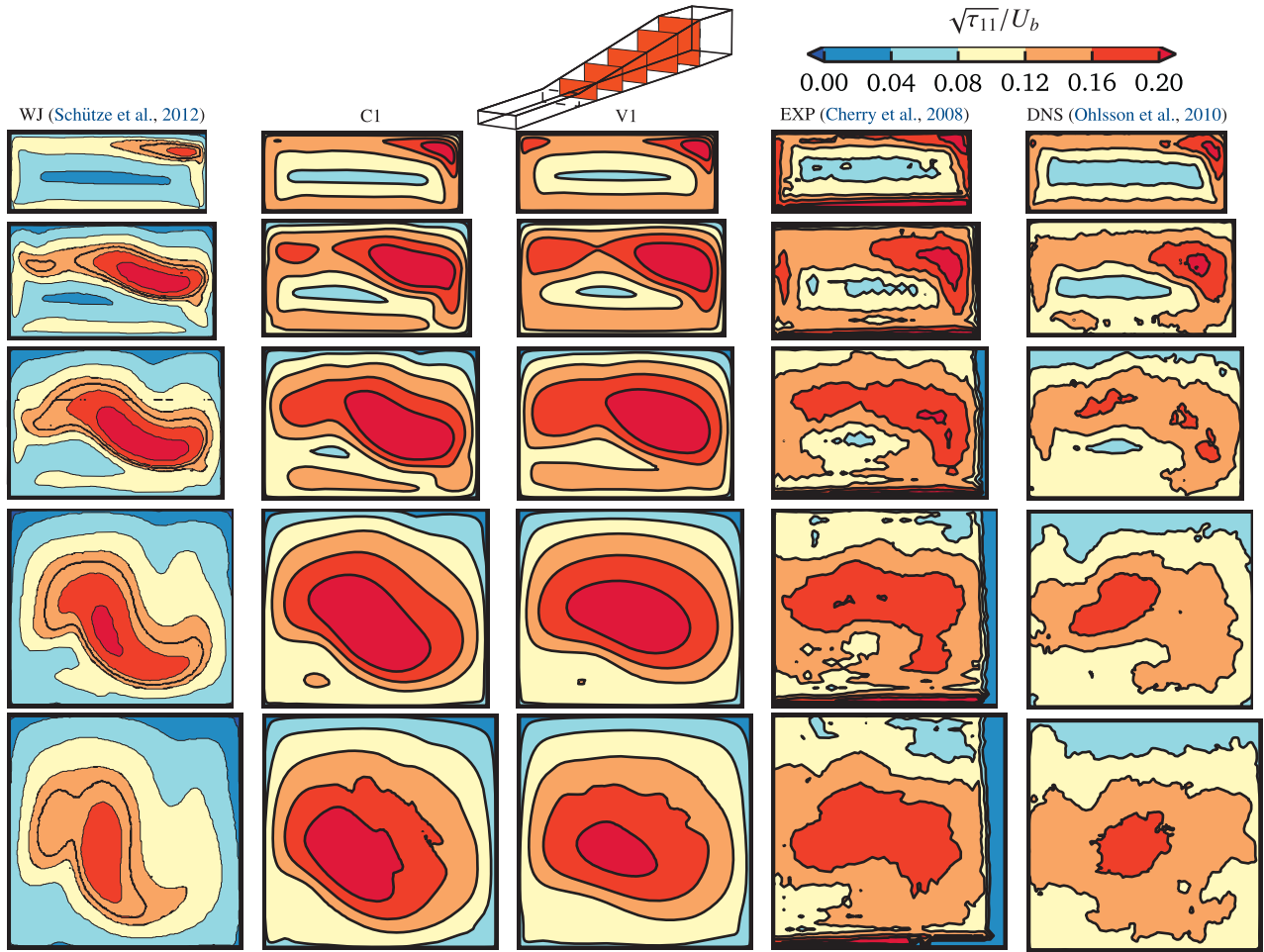
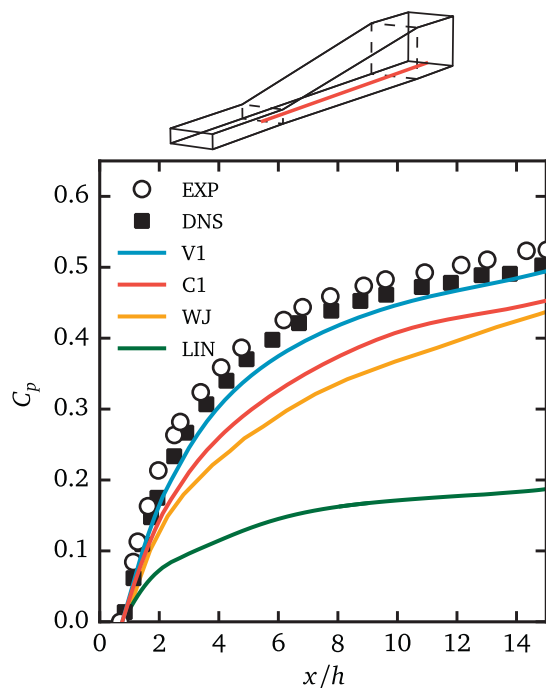
is exciting. Whilst the first comment is obviously stronger than the second, the reader should not take for granted, or underestimate our elation at, the stability of our trained models. We reiterate that no realisability is incorporated in the framework (yet all converging models proved such) and neither is any explicit physics beyond an integrity basis. Naturally, with data-driven turbulence modelling still in its infancy, the full complexity one observes in today's industrial flow problems has not yet been reached. For more complex applications it remains to be seen whether one model could be trained to capture all the physics present in a combustion engine, say. If this proved impossible, then there remains a very plausible alternative — to locally activate different trained closures. This could then spark branches of unified and zonal approaches, much like we see in the H-R/L community (Sagaut et al., 2013). The authors prefer the idea of the former and we speculate the use of further machine-learning methodologies (Ling and Templeton, 2015) to develop identification/blending functions.

The second industrially relevant consideration in this report is using H-R/L to build our training database. Whilst this data contained inaccuracies, the overall flow topology was representative and our conclusion is that this is enough for model training. Steady RANS only resolves flow motions that are present in the mean flow and as such, the database only need contain good information on this. In light of this, it prompts one to postulate new objective functions for optimisation. In this paper we focussed on minimising Eq. (9) and in our previous study (Weatheritt and Sandberg, 2016c) we concentrated on the alignment of the stress tensors predicted by DNS and our models. Both

metrics measure the error in the anisotropy tensor. Perhaps this is not the correct way to get physically intuitive models from data. Instead, considering that this report has largely discussed the vorticity production terms in Eq. (7), perhaps this would be a better objective to match. One can imagine similar ideas considering horseshoe vortices for instance. Our current framework does not account for history effects and propagation of error in our CFD code. Therefore in the diffuser we relied on our models not making errors at the inlet, such small errors could have produced a very different, and less favourable, outcome. Some authors, to circumnavigate this are performing a large series of RANS calculations (in the thousands) and applying Bayes theorem. Results are good, but this is highly expensive, and perhaps, we suggest more sensible objective functions that ensure the closures model physical phenomena, not simply minimise raw error, are a feasible alternative.

Thirdly, from Figs. 14 and 21 it is clear that a non-dimensionalisation by τ_f is inappropriate for the near-wall model because it vanishes. This is an inherent weakness in the modelling assumptions, not the machine-learning algorithm. Perhaps one could investigate a time scale limited by the smallest scales, common to many turbulence models or a transport time scale that is a function of the velocity gradient invariants.

This study has demonstrated another advantage of our symbolic approach. That is we uncovered the functional fragment Eq. (14) as a major contributor to MSV prediction. Therefore, the algorithm has been responsible for uncovering a physical process that is easily explained, yet was not provided or postulated at the outset. The symbolic approach

Fig. 24. Streamwise turbulence intensity at $x/h = 2, 5, 8, 12, 15$ for the DIFF case.Fig. 25. Surface pressure coefficient C_p along the line indicated in the schematic.

also allowed us to modify the production term, to allow for physical solutions. This further highlights a potential need for multi-objective optimisations, that can simultaneously account for momentum diffusion, turbulence energy production and diffusion of the turbulent variables.

Of interest due to the specifics of this study, there are few points to conclude. The prevalence of internal flows means that we hope our models could have an immediate industrial impact. We have been liberal with our inclusion of the trained model equations, such that other researchers can implement and test our closures. We hope that this makes our study one of the easiest machine-learning frameworks to verify, extend and ultimately use the results from. At this stage, we have shown superior results to two existing EASMs for internal flow. A subset of our models can now be applied to further geometries, much like regular turbulence closures are validated using new cases. It would be interesting to get a handle on their absolute robustness. Currently we make no claims about their global scope, our present motivation as outlined in the introduction is to design a universal framework for specific closure formulation and we hope to have persuaded the reader in its viability.

Acknowledgements

The work in this paper has been funded in part by veski and in part by an EPSRC Doctoral Training Centre grant (EP/G03690X/1). This work was also supported by resources provided by The Pawsey Supercomputing Centre with funding from the Australian Government

and the Government of Western Australia. We would also like to thank Ricardo Vinuesa and the KTH group for readily sharing their DNS data.

References

- Abe, K., Jang, Y.-J., Leschziner, M.A., 2003. An investigation of wall-anisotropy expressions and length-scale equations for non-linear eddy-viscosity models. *Int. J. Heat Fluid Flow* 24 (2), 181–198.
- Apsley, D.D., Leschziner, M.A., 1998. A new low-reynolds-number nonlinear two-equation turbulence model for complex flows. *Int. J. Heat Fluid Flow* 19 (3), 209–222.
- Banerjee, S., Krah, R., Durst, F., Zenger, C., 2007. Presentation of anisotropy properties of turbulence, invariants versus eigenvalue approaches. *J. Turbul.* (8), N32.
- Bergeles, G., Gosman, A., Launder, B., 1978. The turbulent jet in a cross stream at low injection rates: a three-dimensional numerical treatment. *Numer. Heat Transfer Part A* (1), 217–242.
- Cherry, E.M., Elkins, C.J., Eaton, J.K., 2008. Geometric sensitivity of three-dimensional separated flows. *Int. J. Heat Fluid Flow* 29 (3), 803–811.
- Cherry, E.M., Elkins, C.J., Eaton, J.K., 2009. Pressure measurements in a three-dimensional separated diffuser. *Int. J. Heat Fluid Flow* 30 (1), 1–2.
- Chien, K.-Y., 1982. Predictions of channel and boundary-layer flows with a low-reynolds-number turbulence model. *AIAA J.* 20 (1), 33–38.
- Craft, T., Iacovides, H., Yoon, J., 2000. Progress in the use of non-linear two-equation models in the computation of convective heat-transfer in impinging and separated flows. *Flow Turbul. Combust.* 63 (1–4), 59–80.
- Daly, B., Harlow, F., 1970. The generalized gradient diffusion hypothesis. *Phys. Fluids* 13, 2634.
- Darwin, C., 1858. On the origin of species by means of natural selection.
- Edeling, W., Cinnella, P., Dwight, R.P., 2014. Predictive RANS simulations via Bayesian model-scenario averaging. *J. Comput. Phys.* 275, 65–91.
- Edeling, W., Cinnella, P., Dwight, R.P., Bijl, H., 2014. Bayesian estimates of parameter variability in the k-e turbulence model. *J. Comput. Phys.* 258, 73–94.
- Ferreira, C., 2001. Gene expression programming: a new adaptive algorithm for solving problems. *Complex Syst.* 13 (2), 87–129.
- Fröhlich, J., Mellen, C.P., Rodi, W., Temmerman, L., Leschziner, M.A., 2005. Highly resolved large-eddy simulation of separated flow in a channel with streamwise periodic constrictions. *J. Fluid Mech.* 526, 19–66.
- Fröhlich, J., von Terzi, D., 2008. Hybrid LES/RANS methods for the simulation of turbulent flows. *Prog. Aerosp. Sci.* 44 (5), 349–377.
- Gatski, T., Speziale, C.G., 1993. On explicit algebraic stress models for complex turbulent flows. *J. Fluid Mech.* 254, 59–78.
- Gessner, F., 1973. The origin of secondary flow in turbulent flow along a corner. *J. Fluid Mech.* 58 (01), 1–25.
- Gullman-Strand, J., Törnblom, O., Lindgren, B., Amberg, G., Johansson, A.V., 2004. Numerical and experimental study of separated flow in a plane asymmetric diffuser. *Int. J. Heat Fluid Flow* 25 (3), 451–460.
- Haller, G., 2005. An objective definition of a vortex. *J. Fluid Mech.* 525, 1–26.
- Hanjalić, K., 2005. Will RANS survive LES? A view of perspectives. *J. Fluids Eng.* 127 (5), 831–839.
- Hunt, J., Savill, A., 2005. Guidelines and criteria for the use of turbulence models in complex flows. *Prediction Turbulent Flows* 291–343.
- Hunt, J.C., Wray, A.A., Moin, P., 1988. Eddies, streams, and convergence zones in turbulent flows. *Center for Turbulence Research Report CTR-S88*.
- Huser, A., Biringen, S., 1992. Direct numerical simulation of turbulent flow in a square duct. *31st Aerospace Sciences Meeting*, pp. 198.
- Jakirlić, S., Jester-Zürker, R., Tropea, C., 2001. Report on the 9th ERCOFTAC/IAHR/COST workshop on refined turbulence modelling. *55 ERCOFTAC Bulletin*. 2001.
- Jakirlić, S., Kadavelil, G., Kornhaas, M., Schäfer, M., Sternel, D., Tropea, C., 2010. Numerical and physical aspects in LES and hybrid LES/RANS of turbulent flow separation in a 3-d diffuser. *Int. J. Heat Fluid Flow* 31 (5), 820–832.
- Kato, M., Launder, B., 1993. The modeling of turbulent flow around stationary and vibrating square cylinders. *Ninth Symposium on Turbulent Shear Flows*, 1993.
- Koza, J.R., 1992. Genetic Programming: On the Programming of Computers by Means of Natural Selection, 1. MIT press.
- Le, N., Xuan, H.N., Brabazon, A., Thi, T.P., 2016. Complexity measures in genetic programming learning: a brief review. *Evolutionary Computation (CEC), 2016 IEEE Congress on*. IEEE, pp. 2409–2416.
- LeCun, Y., Bengio, Y., Hinton, G., 2015. Deep learning. *Nature* 521 (7553), 436–444.
- Leschziner, M., 2015. Statistical Turbulence Modelling for Fluid Dynamics-Demystified: An Introductory Text for Graduate Engineering Students. World Scientific.
- Ling, J., Jones, R., Templeton, J., 2016. Machine learning strategies for systems with invariance properties. *J. Comput. Phys.* 318, 22–35.
- Ling, J., Ruiz, A., Lacaze, G., Oeeflein, J., 2017. Uncertainty analysis and data-driven model advances for a jet-in-crossflow. *J. Turbomach.* 139 (2), 021008.
- Ling, J., Templeton, J., 2015. Evaluation of machine learning algorithms for prediction of regions of high Reynolds averaged Navier Stokes uncertainty. *Phys. Fluids* 27 (8), 085103. (1994–present)
- Ljubojica, M., Rodi, W., 1981. Prediction of horizontal and vertical turbulent buoyant wall jets. *ASME Trans. J. Heat Transfer* 103, 343–349.
- Lumley, J.L., Newman, G.R., 1977. The return to isotropy of homogeneous turbulence. *J. Fluid Mech.* 82 (01), 161–178.
- MacQueen, J., 1967. Some methods for classification and analysis of multivariate observations. *Proceedings of the Fifth Berkeley Symposium on Mathematical Statistics and Probability*. 1. Oakland, CA, USA., pp. 281–297.
- Manceau, R., 2003. Report of the 10th Joint ERCOFTAC (SIG-15)/IAHR/QNET-CFD Workshop on Refined Turbulence Modelling. *57 ERCOFTAC Bulletin*. 2003.
- Menter, F., Garbaruk, A., Egorov, Y., 2012. Explicit algebraic Reynolds stress models for anisotropic wall-bounded flows. *Progress in Flight Physics*. 3. EDP Sciences, pp. 89–104.
- Menter, F.R., 1992. Improved two-equation k-omega turbulence models for aerodynamic flows. *TM 103975*. NASA.
- Menter, F.R., 1994. Two-equation eddy-viscosity turbulence models for engineering applications. *AIAA J.* 32 (8), 1598–1605.
- Moinuddin, K.A., Joubert, P., Chong, M., 2004. Experimental investigation of turbulence-driven secondary motion over a streamwise external corner. *J. Fluid Mech.* 511, 1–23.
- Muldoon, F., Acharya, S., 2006. Analysis of k and epsilon budgets for film cooling using direct numerical simulation. *AIAA J.* 44 (12), 3010–3021.
- Ohlsson, J., Schlatter, P., Fischer, P.F., Henningson, D.S., 2010. Direct numerical simulation of separated flow in a three-dimensional diffuser. *J. Fluid Mech.* 650, 307–318.
- Parish, E.J., Duraisamy, K., 2016. A paradigm for data-driven predictive modeling using field inversion and machine learning. *J. Comput. Phys.* 305, 758–774.
- Parneix, S., Laurence, D., Durbin, P., 1998. A procedure for using DNS databases. *J. Fluids Eng.* 120 (1), 40–47.
- Pichler, R., Sandberg, R.D., Michelassi, V., Bhaskaran, R., 2015. Investigation of the accuracy of RANS models to predict the flow through a low-pressure turbine. *ASME Turbo Expo 2015: Turbine Technical Conference and Exposition*. American Society of Mechanical Engineers. V02BT39A036–V02BT39A036
- Pope, S., 1975. A more general effective-viscosity hypothesis. *J. Fluid Mech.* 72 (02), 331–340.
- Pope, S.B., 1999. A perspective on turbulence modeling. *Modeling Complex Turbulent Flows*. Springer, pp. 53–67.
- Rodi, W., 1976. A new algebraic relation for calculating the Reynolds stresses. *Gesellschaft Angewandte Mathematik und Mechanik Workshop Paris France*. 56.
- Sagaut, P., Deck, S., Terracol, M., 2013. Multiscale and Multiresolution Approaches in Turbulence: LES, DES and Hybrid RANS/LES Methods: Applications and Guidelines. World Scientific.
- Schmitt, F.G., 2007. About boussinesq's turbulent viscosity hypothesis: historical remarks and a direct evaluation of its validity. *Comptes Rendus Mécanique* 335 (9), 617–627.
- Schütze, J., Smirnov, P., Menter, F., 2012. St04: standord 3d diffuser. *ATAAC-Final Workshop 2012-6-11/12 Göttingen*. ANSYS Germany GmbH.
- Sharma, G., Wu, W., Dalal, E.N., 2005. The CIEDE2000 color-difference formula: implementation notes, supplementary test data, and mathematical observations. *Color Res. Appl.* 30 (1), 21–30.
- Simonsen, A., Krogstad, P.Å., 2005. Turbulent stress invariant analysis: clarification of existing terminology. *Phys. Fluids* 17 (8), 088103.
- Spalart, P., Allmaras, S., 1994. A one-equation turbulence model for aerodynamic flows. *Recherche Aéropatiale* 1, 5–21.
- Spalart, P., Shur, M., Strelets, M.K., Travin, A., 2015. Direct simulation and RANS modelling of a vortex generator flow. *Flow Turbul. Combust.* 95 (2–3), 335–350.
- Spalart, P.R., 2000. Strategies for turbulence modelling and simulations. *Int. J. Heat Fluid Flow* 21 (3), 252–263.
- Spalart, P.R., 2009. Detached-eddy simulation. *Annu. Rev. Fluid Mech.* 41, 181–202.
- Spalart, P.R., 2015. Philosophies and fallacies in turbulence modeling. *Prog. Aerosp. Sci.* 74, 1–15.
- Spencer, A., Rivlin, R., 1959. Further results in the theory of matrix polynomials. *Arch. Ration. Mech. Anal.* 4, 214–230.
- Spencer, A.J.M., Rivlin, R.S., 1958. The theory of matrix polynomials and its application to the mechanics of isotropic continua. *Arch. Ration. Mech. Anal.* 2 (1), 309–336.
- Speziale, C.G., Sarkar, S., Gatski, T.B., 1991. Modelling the pressure-strain correlation of turbulence: an invariant dynamical systems approach. *J. Fluid Mech.* 227, 245–272.
- Steeb, W.-H., 2014. *The Nonlinear Workbook: Chaos, Fractals, Cellular Automata, Genetic Algorithms, Gene Expression Programming, Support Vector Machine, Wavelets, Hidden Markov Models, Fuzzy Logic with C++, Java and Symbolic C++ Programs*. World Scientific Publishing Co Inc.
- Steiner, H., Jakirlić, S., Kadavelil, G., Manceau, R., Saric, S., Brenn, G., 2009. 13th ERCOFTAC Workshop on Refined Turbulence Modelling. *79 ERCOFTAC Bulletin*. Graz-university
- Temmerman, L., Leschziner, M.A., 2001. Large eddy simulation of separated flow in a streamwise periodic channel constriction. *2nd Symposium on Turbulence and Shear-Flow Phenomena*, 2001.
- Temmerman, L., Leschziner, M.A., Mellen, C.P., Fröhlich, J., 2003. Investigation of wall-function approximations and subgrid-scale models in large eddy simulation of separated flow in a channel with streamwise periodic constrictions. *Int. J. Heat Fluid Flow* 24 (2), 157–180.
- von Terzi, D., Schneider, H., Bauer, H.-J., 2011. The impact of secondary mean vortices on turbulent separation in 3d diffusers. *High Performance Computing in Science and Engineering'10*. Springer, pp. 339–352.
- Uhlmann, M., Pinelli, A., Kawahara, G., Sekimoto, A., 2007. Marginally turbulent flow in a square duct. *J. Fluid Mech.* 588, 153–162.
- Vinuesa, R., Noorani, A., Lozano-Durán, A., Khouri, G.K.E., Schlatter, P., Fischer, P.F., Nagib, H.M., 2014. Aspect ratio effects in turbulent duct flows studied through direct numerical simulation. *J. Turbul.* 15 (10), 677–706.
- Wallin, S., Johansson, A.V., 2000. An explicit algebraic Reynolds stress model for incompressible and compressible turbulent flows. *J. Fluid Mech.* 403, 89–132.
- Weatheritt, J., Ling, J., Sandberg, R., Saez, G., Bodart, J., 2017. A comparative study of contrasting machine learning frameworks applied to RANS modeling of jets in crossflow. *ASME Turbo Expo 2017: Turbine Technical Conference and Exposition*. American Society of Mechanical Engineers, pp. GT2017-63403.
- Weatheritt, J., Pichler, R., Sandberg, R., Laskowski, G., Michelassi, V., 2017. Machine learning for turbulence model development using a high-fidelity HPT cascade

- simulation. ASME Turbo Expo 2017: Turbine Technical Conference and Exposition. American Society of Mechanical Engineers, pp. GT2017–63497.
- Weatheritt, J., Sandberg, R., 2017. Hybrid Reynolds-averaged/Large eddy simulation methodology from symbolic regression: formulation and application. *AIAA Journal*. Available online:
- Weatheritt, J., Sandberg, R.D., 2015. Use of symbolic regression for construction of Reynolds-stress damping functions for hybrid RANS/LES. 53rd AIAA Aerospace Sciences Meeting. 2015–0312
- Weatheritt, J., Sandberg, R.D., 2016. Hybrid simulation of the surface mounted square cylinder. 20th Australasian Fluid Mechanics Conference.
- Weatheritt, J., Sandberg, R.D., 2016. A new Reynolds stress damping function for hybrid RANS/LES with an evolved functional form. Advances in Computation, Modeling and Control of Transitional and Turbulent Flows. World Scientific, pp. 330–339.
- Weatheritt, J., Sandberg, R.D., 2016. A novel evolutionary algorithm applied to algebraic modifications of the RANS stress-strain relationship. *J. Comput. Phys.* 325, 22–37.
- Weinmann, M., Sandberg, R., 2009. Suitability of explicit algebraic stress models for predicting complex three-dimensional flows. 19th AIAA Computational Fluid Dynamics. pp. 3663.
- Weinmann, M., Sandberg, R.D., Doolan, C., 2014. Tandem cylinder flow and noise predictions using a Hybrid RANS/LES approach. *Int. J. Heat Fluid Flow* 50, 263–278.
- Weller, H.G., Tabor, G., Jasak, H., Fureby, C., 1998. A tensorial approach to computational continuum mechanics using object-oriented techniques. *Comput. Phys.* 12 (6), 620–631.
- Wilcox, D.C., 1993. Turbulence modeling for CFD. 2 DCW industries, Inc, La Canada, CA.
- Xiao, H., Wu, J.-L., Wang, J.-X., Sun, R., Roy, C., 2016. Quantifying and reducing model-form uncertainties in Reynolds-Averaged Navier–Stokes simulations: a data-driven, physics-informed Bayesian approach. *J. Comput. Phys.* 324, 115–136.